

PHYSICAL PROPERTIES OF LAMINAR HELIUM DEFLAGRATIONS

F. X. TIMMES

Center on Astrophysical Thermonuclear Flashes, Enrico Fermi Institute, University of Chicago, Chicago, IL 60637; fxt@burn.uchicago.edu

Received 1999 April 4; accepted 1999 August 20

ABSTRACT

The physical properties of laminar deflagrations propagating through helium-rich compositions are determined for a wide range of temperatures and densities. The speeds, thermal widths, reactive widths, density contrasts, critical temperatures, and trigger masses are analyzed, along with their sensitivity to the input thermal transport coefficients, nuclear reaction rates, nuclear reaction network employed, and equation of state. A simple fitting formula of modest accuracy for the laminar flame speed is given, as well as detailed tables that list all of the physical properties. These physical properties may be incorporated into hydrodynamic programs as subgrid models for flame-tracking algorithms, and have applications toward models of X-ray bursts and the thin-shell helium flash of intermediate-mass stars.

Subject headings: hydrodynamics — methods: numerical —

nuclear reactions, nucleosynthesis; abundances — stars: interiors

1. INTRODUCTION

Thermonuclear flame fronts arise in a number of stellar situations. In some of these situations, the flame front operates in a layer that is thin compared to the radius of the star. Local temperature perturbations in these thin layers become amplified as a result of the extreme nonlinear temperature dependence of the nuclear reaction rates. As such, the flame fronts in these thin layers are probably born at an individual point, or a small set of points, rather than simultaneously throughout the entire layer, as spherically symmetric models require. The flame front which propagates through the thin layer may either be a detonation, which travels faster than the local sound speed, or a deflagration, which is subsonic. Which type of flame front initially propagates depends primarily on the initial thermodynamic conditions. Once such a point detonation or deflagration is born, it then propagates both laterally around the star and vertically through the layer. The observed rise time of the luminosity or the duration of an event may be related in a fundamental way to the speed at which the flame front propagates through the thin layer.

Two examples where such thermonuclear flame fronts play a role are in models of X-ray bursts and the thin-shell helium flashes of intermediate-mass stars.

Neutron stars that accrete hydrogen-rich material from a binary companion, or from the interstellar medium, end up with a thin layer of helium-rich fuel on their surface. The helium-rich fuel may be spread evenly over the entire neutron star, or may be confined to the polar regions if the magnetic field is sufficiently strong. For layers where the density at the base of the accreted layer reaches $\sim 10^8$ g cm $^{-3}$ and the temperature reaches $\sim 1.2 \times 10^8$ K before the flame front is born, a detonation probably develops. If so, the detonation front propagating in the lateral direction (perpendicular to the direction of the gravitational force) moves at the Chapman-Jouguet speed of $\sim 10^9$ cm s $^{-1}$. For layers where the density at the base of the accreted layer is less than $\sim 10^7$ g cm $^{-3}$ before the flame front is born, a deflagration probably develops. The lateral speed of the laminar deflagration is roughly 10^4 cm s $^{-1}$. The vast difference between these estimates for the detonation speed and the deflagration speed imply very different predictions for

the rise time of an X-ray burst (e.g., Fryxell & Woosley 1982).

The thin-shell helium flash that occurs during the advanced evolutionary stages of intermediate-mass stars (Schwarzschild & Härm 1965) results from the initial nuclear burning being unable to raise the overlying hydrogen envelope sufficiently to extinguish the reactions. A drastic temperature rise at near-constant pressure ensues. Shortly after reaching its peak temperature, however, the material does expand and cool rapidly. Note that in contrast to the neutron star example, the layer of fuel in the thin-shell helium flash is located inside the star rather than on the surface of the star. Average densities at the onset of the thin-shell helium flash are $\sim 10^4$ g cm $^{-3}$ and average temperatures are $\sim 2 \times 10^8$ K, and a deflagration probably develops. For such thermodynamic conditions the laminar deflagration propagates at ~ 5 cm s $^{-1}$. Fryxell & Woosley (1982) estimate that the entire thin shell may or may not undergo an essentially spherically symmetric ignition, depending on how much the laminar deflagration speed is increased by turbulent motions within the thin shell.

The physical properties of helium detonations appear to be well characterized (Mazurek 1973; Khokhlov 1988), but the physical properties of helium deflagrations have not been as well characterized. Either simple order-of-magnitude estimates (Fryxell & Woosley 1982) or detailed calculations over a restricted range of initial conditions (Bildsten 1995) are found in the literature. It is of pragmatic importance to complete the physical properties of helium flame fronts by knowing the correct characteristics of helium deflagrations over a wide range of initial conditions.

The primary purpose of this paper is to provide a systematic and quantitative evaluation of the physical properties of subsonic, laminar flame fronts propagating through helium-rich compositions. In this class of flame fronts, the propagation of a self-sustained burning front is determined by a balance between nuclear energy generation and thermal transport. The physical properties (speed, thermal width, reactive width, density contrast, critical temperature, and trigger mass) of these helium deflagrations are calculated for three different compositions (variations in the helium and carbon abundances) on a grid of densities

between 10^4 and 10^8 g cm $^{-3}$ and temperatures between 4×10^7 and 3×10^8 K. Although the development of a detonation instead of deflagration is the more widely held view for densities greater than $\sim 10^7$ g cm $^{-3}$, a well-founded consensus has yet to emerge, and it would be rash to assert that the possibility of a deflagration is precluded. As such, the physical properties of deflagrations for densities greater than $\sim 10^7$ g cm $^{-3}$ are included in this survey.

The flame speed of a self-sustained laminar deflagration is special because it is the absolute slowest speed at which a subsonic burning front can propagate. Even so, a strictly laminar flame is almost a complete fantasy under most astrophysical conditions because turbulence or convection generally prevails at the conditions where deflagrations occur. A laminar deflagration is also subject to many different types of hydrodynamic instabilities. In addition, the width of a laminar deflagration can be tiny compared to the stellar dimensions. For example, at a density of $\sim 10^7$ g cm $^{-3}$ and a temperature of $\sim 10^8$ K, the reactive width of the laminar flame speed is ~ 0.5 cm. For a neutron star radius of 10 km, this means a dynamic range in linear size of more than 10^6 . Resolving the reactive width of the helium deflagration while carrying the entire neutron star is not feasible in multidimensional calculations, even with current adaptive mesh-refinement algorithms.

As a result of these difficulties, parameterized expressions which attempt to describe how bulk fluid motions or various hydrodynamic instabilities increase the speed of burning front over and above the laminar flame speed. Almost all of these formulae for the speed of a subsonic burning front propagating through turbulent or convectively unstable material have, for good physical reasons, the laminar flame speed in their expressions. In some regimes the turbulent deflagration speed is basically independent of the laminar flame speed (Khokhlov 1995; Niemeyer & Hillbrandt 1995a, 1995b; Timmes & Niemeyer 1999). In other regimes there is a tasteful dependence on the laminar flame speed. It is thus of some interest to those who apply such parameterized turbulent burning expressions in their stellar models to have reasonably precise values for the laminar flame speed. Hence, the main utility of the laminar flame calculations presented in this work will probably be to incorporate the tabulated properties into hydrodynamic programs as subgrid models for flame-tracking algorithms. The calculated properties can also find utility in refining order-of-magnitude estimates and scaling relations.

In § 2 the computational methods and the input physics used to determine the physical properties of conductive, burning nuclear flames are discussed. In § 3 the physical properties of helium deflagrations, their sensitivity to the input physics, and comparisons to previous calculations are presented. Finally, a summary of the results is given in § 4.

2. PROCEDURE

The theoretical framework for laminar deflagrations in astrophysical situations is described in Timmes & Woosley (1992). The salient points as applied to laminar helium deflagrations are briefly summarized for completeness.

Let isotope i have Z_i protons and A_i nucleons (protons + neutrons). Let the aggregate total of isotope i have a number density n_i (in cm $^{-3}$) in material with a temperature T (in K) and a mass density ρ (in g cm $^{-3}$). Define the mass fraction (dimensionless) of isotope i as $X_i = \rho_i/\rho = n_i A_i/(\rho N_A)$, where N_A is Avogadro's number, and define the

molar abundance of isotope i as $Y_i = n_i/n = X_i/A_i$. Mass conservation is then expressed by

$$\sum_{i=1}^N X_i = 1. \quad (1)$$

This summation should be checked at every time step for every zone in a helium deflagration model. Failure to satisfy equation (1) to the limiting precision of the arithmetic may manifest itself in the unphysical buildup (or decay) of the energy generation rate, and the entire model may suffer inaccuracies if mass conservation is significantly violated over sufficiently long timescales.

Figures of merit for the effectiveness of mass diffusion and shear viscosity are provided by the dimensionless Lewis and Prandtl numbers. The Lewis number is the ratio of thermal energy transport to mass transport,

$$\text{Le} = \frac{\text{thermal transport}}{\text{mass transport}} = \frac{\sigma}{\rho C_p D} \approx \frac{10^{17}}{10^6 10^8 10^{-2}} \approx 10^5, \quad (2)$$

where σ is the thermal conductivity, C_p is the specific heat at constant pressure, and D is the mass diffusion coefficient (estimated from Paquette et al. 1986). The Prandtl number is the ratio of viscous momentum transport to thermal energy transport,

$$\text{Pr} = \frac{\text{viscous transport}}{\text{thermal transport}} = \frac{C_p \eta}{\sigma} \approx \frac{10^8 10^5}{10^{17}} \approx 10^{-4}, \quad (3)$$

where η is the shear viscosity (estimated from Nandkumar & Pethick 1984). To an excellent approximation then, the mass diffusion and shear viscous processes are not important for helium deflagrations. In addition, it is implicitly assumed that the material through which the laminar deflagration propagates is quiescent; the Reynolds number is close to zero, so the material is neither turbulent or convective.

Laminar deflagrations propagate with a steady state speed V_{cond} that is a small fraction of the ambient sound speed ($V_{\text{cond}}/c_s \ll 1$). Since all of the material is in causal contact by sound waves, the pressure ahead of the steady state burning front is equal to the pressure of the incinerated material behind the flame front. Thus, deflagrations operate in an isobaric environment. This allows the momentum equation to be dropped from the general reactive fluid flow equations, and results in a considerable simplification of the calculation.

Under the assumptions of negligible mass diffusion, insignificant shear viscosities, and quiescent material in an isobaric environment, the physical properties of helium deflagrations may be evaluated by solving the coupled diffusion-reaction equations:

$$\begin{aligned} \frac{dE}{dt} + P \frac{d(1/\rho)}{dt} &= \frac{1}{\rho} \frac{d}{dx} \left(\sigma \frac{dT}{dx} \right) + \dot{S}, \\ \dot{S} &= N_A \sum_{j=1}^N \frac{dY_i}{dt} B_j - \dot{S}_v, \\ \frac{dY_i}{dt} &= \sum_{j,k} Y_i Y_k \lambda_{kj}(I) - Y_i Y_j \lambda_{jk}(I). \end{aligned} \quad (4)$$

In these reaction-diffusion equations, the specific thermal energy is E (in ergs g $^{-1}$), the scalar pressure is P (in ergs

cm^{-3}), the nuclear energy generation rate is \dot{S} (in ergs g^{-1}), the neutrino energy loss rate is \dot{S}_ν , the binding energy of isotope i is B_i , and the binary reverse (creation) and forward (destruction) nuclear reaction rates are λ_{kj} and λ_{jk} . The thermal conductivity σ (in $\text{ergs cm}^{-1} \text{K}^{-1} \text{s}^{-1}$) due to radiative and conductive processes is

$$\sigma = \sigma_{\text{rad}} + \sigma_{\text{cond}} = \frac{4acT^3}{\rho} \left(\frac{1}{\kappa_{\text{rad}}} + \frac{1}{\kappa_{\text{cond}}} \right), \quad (5)$$

where c is the speed of light, a is related to the Stefan-Boltzmann constant by $\sigma_B = ac/4$, and κ is the opacity (in $\text{cm}^2 \text{g}^{-1}$). Note that $P dV$ work is retained in the thermal energy equation. Closure of the reactive flow equations is enforced by the equation of state $P = P(\rho, T, X)$ and $E = E(\rho, T, X)$, where $X = (X_1, X_2, X_3, \dots)$ are the mass fractions.

The nonlinear reaction-diffusion equations are solved by Newton-Raphson iteration on the implicit Crank-Nicholson differencing scheme. An adaptive mesh-refinement algorithm which attempts to produce a uniform distribution of arc lengths $ds^2 = dx^2 + dT^2$ is used; that is, zones are added, deleted, and refined as the flame propagates. This strategy alleviates the need to specify a complete region for the simulation before the computation even commences. It also has the practical benefit of saving substantial amounts of computer time and storage space. A Dirichlet

boundary condition $T = T_{\text{upstream}}$, representing a constant upstream temperature, is imposed on the right boundary. A Neumann boundary condition $dT/dx = 0$, representing zero heat flux, is imposed on the left boundary. A perturbing step function in temperature is taken as the initial condition, and the steady state properties of the resulting deflagration wave are sought.

An example of this type of calculation is shown in Figure 1. Starting with a region of pure helium at a density of 10^6 g cm^{-3} and a temperature of 10^8 K , the perturbing temperature step function (red line on the left) is sufficiently large enough to ignite the material. A deflagration begins to propagate as the energy released by the nuclear reactions is transported into the upstream material by conductive processes. The temperature profiles in Figure 1 are spaced 2000 time steps apart, which is nearly equal spacing in time. The spatial grid used for each temperature profile is represented by the open circles. After the initial transient behavior dies away, a steady state deflagration propagates into the upstream material. For this upstream composition and these thermodynamic conditions, the helium deflagration propagates with a steady state speed of 853 cm s^{-1} . The thermal width of the flame, defined as the distance between the points where the temperature reaches 90% and 10% of its maximum, is 831 cm. The reactive width of the flame zone, defined as the distance between the points where the nuclear energy generation rate reaches 90% and 10% of its

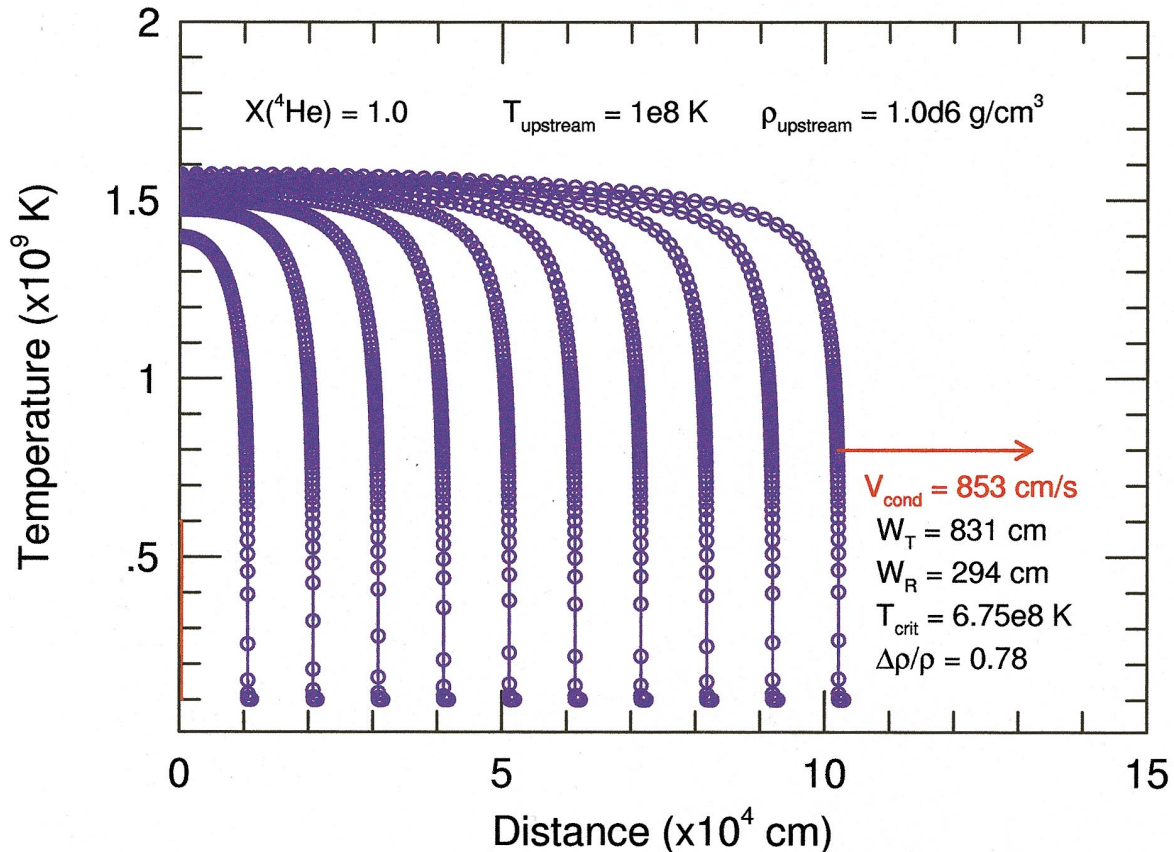


FIG. 1.—Temperature evolution of a laminar deflagration propagating into a region of pure helium at a density of 10^6 g cm^{-3} and a temperature of 10^8 K . Starting from a temperature step function (red line on the left), a steady state deflagration front propagates. The temperature profiles are spaced 2000 time steps apart, which is approximately equal spacing in time. The grid used in the calculation is represented by open circles. This helium deflagration propagates into the upstream material at a speed of 853 cm s^{-1} and has a thermal width of 831 cm, a reactive flame zone width of 294 cm, a critical temperature of $6.75 \times 10^8 \text{ K}$, and a density contrast between the upstream density and the density behind the flame front of 0.78. The entire region plotted comprises about 10^{22} g of material.

maximum value, is 294 cm. The critical temperature of the flame, defined as the temperature along the flame front where heating due to nuclear reactions exactly equals the cooling due to thermal conduction, is 6.75×10^8 K. The mass density of material located behind the flame front is smaller than the mass density of material ahead of the flame front because of the isobaric property of deflagrations. The density contrast $\Delta\rho/\rho$ between the upstream density and the density behind the flame front in Figure 1 is 0.78. The entire region shown in Figure 1 comprises about 10^{22} g, or about $10^{-11} M_\odot$ of material.

The time evolution and analysis done for Figure 1 was repeated for 525 different initial conditions: 25 upstream densities between 10^4 and 10^8 g cm $^{-3}$, seven upstream temperatures between 4×10^7 and 3×10^8 K, and compositions of pure helium, half helium and half carbon, and 30% helium and 70% carbon. Most of these calculations were repeated with different equations of state, conductivity multipliers, nuclear reaction networks, and nuclear reaction rates to determine the sensitivity of the steady state properties to the input physics.

Before discussing the key pieces of physics that determine the properties of helium deflagrations in the next section, it is worth recording the order-of-magnitude estimate for the steady state speed and thermal width of a deflagration:

$$V_{\text{cond}} \sim \left(\frac{c\dot{S}}{\kappa\rho\dot{S}} \right)^{1/2}, \quad W_T \sim \left(\frac{cE}{\kappa\rho\dot{S}} \right)^{1/2}. \quad (6)$$

Although based on dimensional analysis (equality of the burning and diffusion timescales) and not very accurate in an absolute sense, equation (6) does provide reasonably accurate scaling relations and insight into the behavior of a deflagration's steady state properties.

2.1. Equation of State

The accuracy, thermodynamic consistency, and execution speed of five different equation-of-state routines that are used in modeling stellar events is analyzed in Timmes & Arnett (1999). The equation-of-state routines examined in their survey encompass one that is exact (for the assumptions imposed) in IEEE 64 bit arithmetic and served as a reference point for the other equations of state. The other four equations of state analyzed in their survey are one written by Iben primarily for evolving models of intermediate- and low-mass stars (Iben et al. 1992), one composed by Weaver, Zimmerman, & Woosley (1978) chiefly for evolving models of massive stars, one summarized by Nadyozhin (1974) and explained in detail by Blinnikov et al. (1996), and one developed by Arnett (1996) chiefly for use in multidimensional hydrodynamic simulations.

An electron-positron equation of state based on table interpolation of the Helmholtz free energy $F(\rho, T)$ is developed and analyzed in Timmes & Swesty (1999). The interpolation scheme guarantees thermodynamic consistency to the limiting precision of the arithmetic, independent of the chosen interpolating function. The choice of a biquintic Hermite polynomial as the interpolating function results in accurately reproducing the underlying Helmholtz free-energy data in the table, and yields derivatives of the pressure, specific entropy, and specific internal energy, which are smooth and continuous. In addition, the interpolation in just two dimensions (temperature and density) is valid for

any composition. Separate planes for each composition are neither necessary nor desirable, since simple multiplication or division by the composition variables in the appropriate places gives the desired composition scaling.

The analysis performed by Timmes & Arnett (1999) and Timmes & Swesty (1999) permits a complete assessment of the six equation-of-state routines described above, and allows a few practical guidelines to be suggested. If maintaining absolute accuracy and thermodynamic consistency is the primary concern, then there is no substitute for calculating the Fermi-Dirac functions to high precision, reducing the uncertainty in the value of η from the root find to the limits of the arithmetic, obtaining analytic partial derivatives, and entering values of the fundamental physical constants to their recommended precision. A downside to this approach is a significant increase in the CPU resources needed to model a stellar event, including helium deflagrations. When an optimal balance between accuracy, thermodynamic consistency, and speed is desirable, then the Helmholtz free-energy equation of state operating in pipeline mode is a strong choice. A downside to this approach is that attention must be given to ensure that all phase transitions (e.g., positron production) are adequately resolved by the chosen table density.

All six of the equation-of-state routines described above were used during the laminar helium deflagration calculations, especially during the analysis of the sensitivity of the results to the chosen equation of state. The bulk of the evaluations were done, however, with the Helmholtz equation of state.

All of the state routines take as input the temperature T , density ρ , the mean number \bar{A} of nucleons per isotope, and the mean charge \bar{Z} per isotope. Each equation-of-state routine then returns as output the scalar pressure P (in ergs cm $^{-3}$), specific thermal energy E (in ergs g $^{-1}$), and the thermodynamic derivatives of these quantities with respect to the density and temperature. For helium deflagrations, the isobaric pressure is given instead of the density as the basic input. Obtaining the density by iteration can be a significant portion of the computational cost in cases where the number of isotopes being evolved is relatively small.

The $\rho - T$ plane of Figure 2 shows the operating region of pure helium deflagrations as the yellow polygon. Regions to the right of the vertical dashed line at 7×10^6 g cm $^{-3}$ are strongly influenced by relativistic effects ($p_e c \sim 2m_e c^2$, where p_e is the electron Fermi momentum), while regions to the left of the line are essentially nonrelativistic. Regions above the black dashed line, which starts at $\sim 10^7$ K, are influenced by degeneracy effects (nondegenerate electron pressure \sim nonrelativistic degenerate electron pressure, $\rho \sim 2.4 \times 10^{-8} T^{3/2}$), while regions below the line are essentially nondegenerate. Regions above the solid black line are generally in the liquid phase, while regions below this line are typically in the solid phase ($\Gamma = \bar{Z}^2 e^2 / akT \gtrsim 170$, where a is the average ion-ion separation). The solid orange line indicates where the radiative opacity equals the thermal conductive opacity. Areas below the solid line have flame dynamics that are dominated by electron thermal conduction, while regions above the solid orange line are dominated by the opacity of radiative processes. The solid red line shows the critical temperature of deflagrations in pure helium. The critical temperature is analyzed in detail in § 3, but it is essentially the temperature where nuclear energy generation equals the diffusion of energy (heating equals

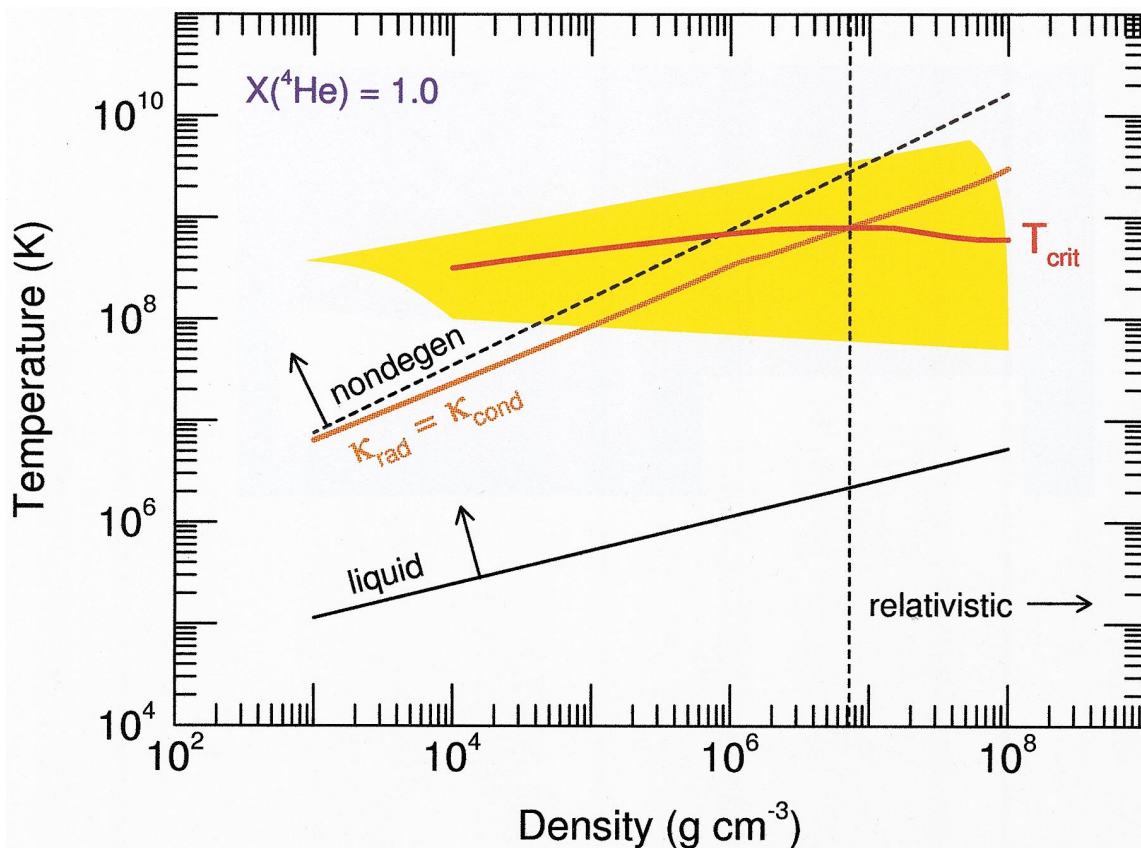


FIG. 2.—Operating region of helium deflagrations (yellow polygon) in the ρ - T plane. Regions to the right of the vertical dashed line are affected by relativity, areas above the black dashed line which starts at $\sim 10^7$ K are largely degenerate, and regions above the solid black line generally correspond to the liquid phase of matter. Areas above the solid orange line and thermal-transport coefficients dominated by radiative processes, while below the orange line conductive processes dominate. The solid red line shows the critical temperature, essentially where heating equals cooling along the flame front. The yellow polygon indicates that helium deflagrations always operate in the liquid regime but traverse all possible combinations of relativistic degeneracy and all types of dominant thermal-transport mechanisms.

cooling) along the flame front. The yellow polygon in Figure 2 indicates that helium deflagrations always operate in the liquid regime, but traverse all possible relativistic, degenerate, conductive, and radiative regions. Models of laminar helium deflagrations thus require a rich set of physics to adequately describe their physical properties. Laminar deflagrations propagating through carbon-oxygen compositions are somewhat simpler because the astrophysical conditions of interest (Type Ia supernovae) dictate that the laminar flame fronts almost always operate in regions dominated by relativistic and degenerate thermodynamics and thermal conductivities (see Fig. 5 of Timmes & Woosley 1992). Part of the richer set of physics required by helium deflagrations are the thermal transport properties, a subject which is addressed next.

2.2. Thermal Transport

Thermal transport is the most crucial transport property to model for laminar deflagrations, since mass diffusion and shear-viscosity processes are not significant (large Lewis and small Prandtl numbers, respectively). Heat generated by nuclear reactions in the flame zone of a steady state helium deflagration is transported upstream into the cold material by conductive and radiative processes. At the largest upstream densities and coldest upstream temperatures considered in this study, thermal transport by conduction dominates over the radiative processes. At the

smallest upstream densities and hottest upstream temperatures considered, radiative processes dominate the transport of thermal energy. At intermediate upstream densities and temperatures, both conductive and radiative processes contribute. Accordingly, both radiative and conductive transport processes need to be considered.

Analytic fits from Iben (1975) and Christy (1966) are used for the radiative opacity when all processes other than electron scattering are considered. An approximation formula from Weaver et al. (1978) for the Compton opacity, which includes a cutoff for frequencies less than the plasma frequency, is then added to form the total radiative opacity. Analytic fits from Iben (1975) are used for the thermal conductivity in the nondegenerate regime. In the degenerate regime, the thermal conductivity formalism of Yakovlev & Urpin (1980) is used. In this approach, contributions from ion-electron, electron-electron, and phonon-electron scattering are summed to form the total thermal conductivity. Potekhin, Chabrier, & Yakovlev (1997) give an approximation formula for the electron-electron interaction integral $J(y)$ that is more complete than the approximation formula given by Timmes (1992). A smooth and continuous interpolation function joins the thermal conductivity expressions in the degenerate and nondegenerate regimes in the transition regions. The radiative opacity is converted to an equivalent conductivity by $\sigma_{\text{rad}} = 4acT^3/(3\rho\kappa_{\text{rad}})$ before forming the total thermal conductivity. Solving for the loca-

tions where the radiative contribution equals the thermal contribution gives the solid orange line in Figure 2. The Appendix A lists the FORTRAN routine used in this paper to determine the thermal transport properties appropriate for evaluating the physical properties of the helium deflagrations.

2.3. Nuclear Reaction Networks

Methods for solving the stiff system of ordinary differential equations that constitute nuclear reaction networks are surveyed in Timmes (1999). The scaling properties and behavior of three semi-implicit time-integration algorithms and eight linear algebra packages are investigated by running each of these 24 combinations on seven different nuclear reaction networks. The ensuing analysis permits a full assessment of the integration methods and linear algebra packages surveyed, and allows several pragmatic suggestions to be offered. When a balance between accuracy, overall efficiency, memory footprint, and ease of use is desirable, then the variable-order Bader-Deufhard time-integration method coupled with the MA28 sparse-matrix package is a good choice.

The energy released by nuclear reactions \dot{S} and the resulting nucleosynthesis of helium deflagrations are obtained by integrating five different nuclear reaction networks: (1) a 2 isotope network that converts helium to carbon by the triple- α reaction, (2) a 3 isotope network that converts helium to carbon and oxygen by the triple- α and

$^{12}\text{C}(\alpha, \gamma)^{16}\text{O}$ reaction, (3) a 19 isotope network that covers the α -chain isotopes from helium to nickel and includes the heavy-ion reactions, (4) a 47 isotope network that removes the steady state linkages assumed in the 19 isotope network, and (5) a 127 isotope network. Table 1 lists the isotopes included in each of the five networks, and the last three networks are described in detail in the Timmes (1999) survey. Using all five of these nuclear reaction networks permits a reasonable sensitivity analysis of the flame's physical properties on the assumed nuclear reaction network.

The tabulation of Caughlan & Fowler (1988) was employed for most of the key nuclear reaction rates. Modern values for some of the reaction rates were taken from the reaction rate library of R. Hoffman (1999, private communication). Nuclear reaction rate screening effects as implemented by Wallace, Woosley, & Weaver (1982) and decreases in the energy generation rate \dot{S} due to neutrino losses as given by Itoh et al. (1996) were included in the calculations. In general, the neutrino loss rates are small enough to have almost no effect on the steady state properties of helium deflagrations.

3. RESULTS

The steady state speed of deflagrations propagating through a pure helium composition is shown in Figure 3, a half-helium and half-carbon composition in Figure 4), and a composition of 30% helium and 70% carbon in Figure 5).

TABLE 1
NUCLEAR REACTION NETWORKS

ELEMENT	Net 1 (2) ^a		Net 2 (3)		Net 3 (19)		Net 4 (47)		Net 5 (127)	
	A_{\min}	A_{\max}	A_{\min}	A_{\max}	A_{\min}	A_{\max}	A_{\min}	A_{\max}	A_{\min}	A_{\max}
n	1	1	1	1	1	1
H	1	1	1	3	1	3
He	4	4	4	4	3	4	3	4	3	4
Li	6	7
Be	7	9
B	8	11
C	12	12	12	12	12	12	12	13	12	14
N	14	14	13	15	13	15
O	16	16	16	16	16	18	16	19
F	18	19	18	21
Ne	20	20	20	20	19	24
Na	23	23	20	24
Mg	24	24	23	24	23	27
Al	27	27	25	29
Si	28	28	27	28	27	32
P	30	31	29	32
S	32	32	31	32	30	34
Cl	35	35	33	37
Ar	36	36	36	36	35	39
K	39	39	37	42
Ca	40	40	40	40	39	44
Sc	43	43	42	46
Ti	44	44	44	44	43	49
V	47	47	46	51
Cr	48	48	48	48	47	52
Mn	51	51	49	55
Fe	52	54	52	52	47	63
Co	55	55	50	65
Ni	56	56	56	56	54	60

NOTE.— A -mass number.

^a Numbers in parentheses are numbers of isotopes in the network.

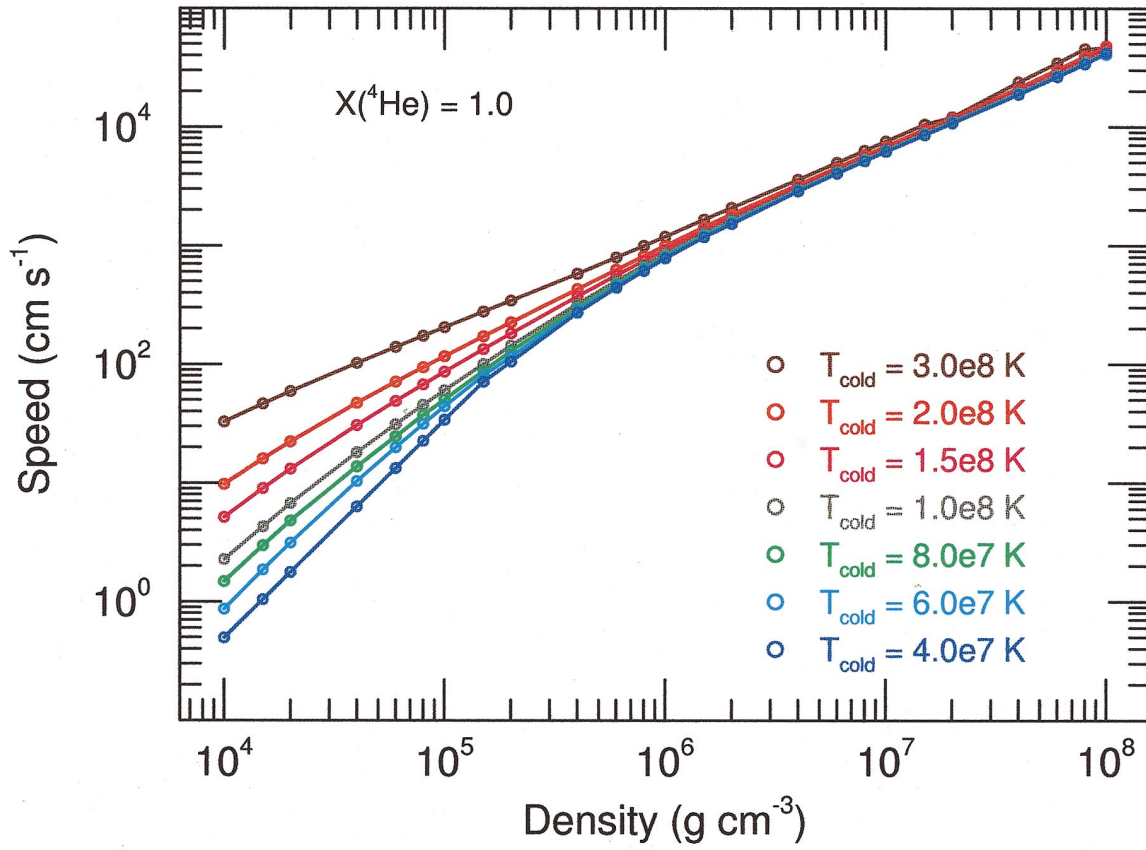


FIG. 3.—Steady state speed of a laminar deflagration propagating into pure helium. The upstream density is given on the x-axis and the speed on the y-axis. Each labeled colored curve corresponds to a different upstream temperature. The deflagration speeds depend on both the upstream density and the temperature because the material is nondegenerate.

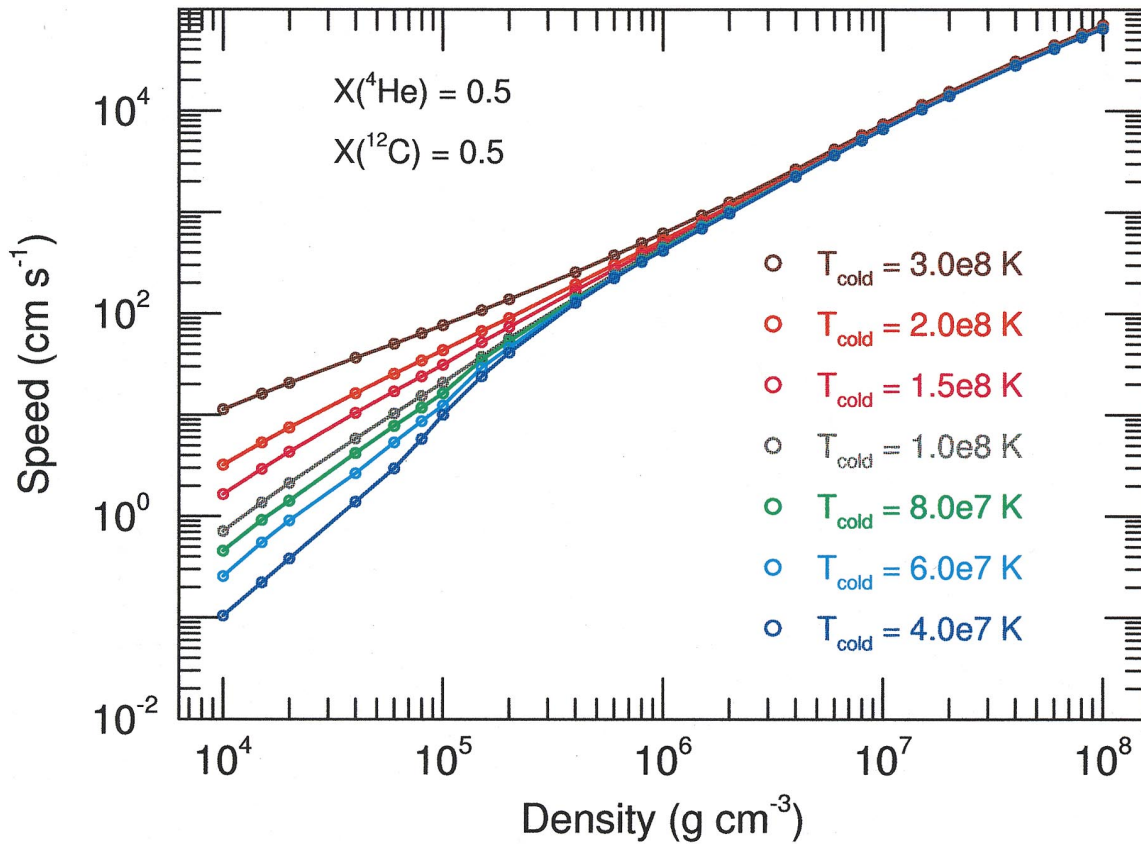


FIG. 4.—Steady state speed of a laminar deflagrations propagating into a half-helium $X(^4\text{He}) = 0.5$ and half-carbon $X(^{12}\text{C}) = 0.5$ mixture. The format is the same as in Figure 3.

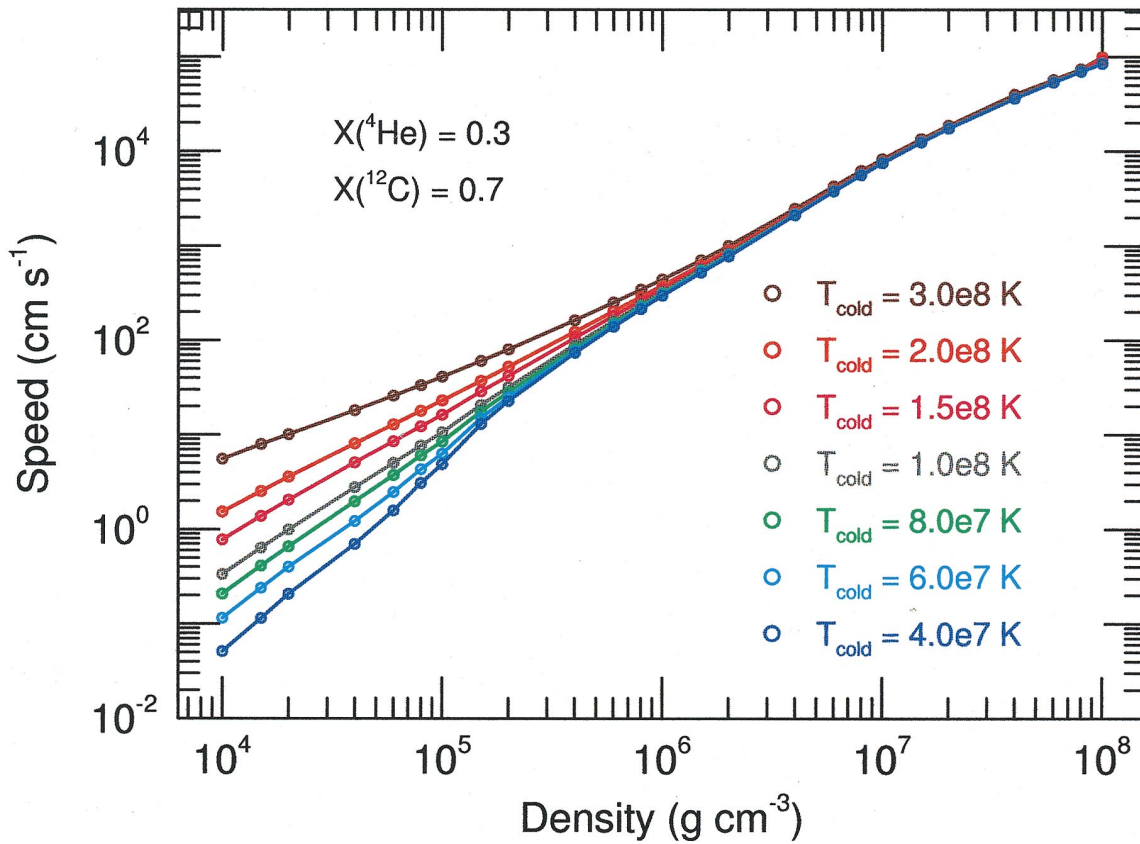


FIG. 5.—Steady state speeds of laminar deflagrations propagating into a 30% helium and 70% carbon mixture. The format is the same as in Figure 3.

The x -axis gives the upstream mass density, the y -axis the deflagration speed, and each colored curve corresponds to a different upstream temperature. All three compositions are largely degenerate at upstream densities greater than $\sim 10^6 \text{ g cm}^{-3}$, and become more degenerate as the density increases. This is why the flame speeds are essentially independent of the upstream temperature in this region of Figures 3–5. At these densities, the physical properties of helium deflagrations are controlled by the thermal conductivity of the degenerate, relativistic electrons. All three compositions are largely nondegenerate, at densities less than $\sim 2 \times 10^6 \text{ g cm}^{-3}$, and behave more as an ideal gas as the density decreases. Thus, the flame speeds depend on both the upstream density and the temperature in this region of Figures 3–5. At these thermodynamic conditions, the physical properties of helium deflagrations are controlled by the radiative transport of energy (also see Fig. 2).

A comparison of the flame speeds for the three compositions at an upstream temperature of 10^8 K is shown in Figure 6. The x -axis gives the upstream mass density, the y -axis the deflagration speed, and each colored curve corresponds to one of the labeled compositions. All three compositions have flame speeds that monotonically increase with the upstream density. The rate of increase is different for each composition, resulting in the curves crossing each other at a density of $\sim 7 \times 10^6 \text{ g cm}^{-3}$. Pure helium deflagrations have the fastest speeds below this confluence point, while the composition with the largest carbon abundance has the fastest flame speeds above this confluence point.

The existence of the confluence point in Figure 6 and the different behaviors on either side of the confluence point is due to helium burning consisting of two reactions; the

triple- α reaction and the $^{12}\text{C}(\alpha, \gamma)^{16}\text{O}$ reaction. Neglecting screening factors and higher order resonances, the energy generation rate due to these two reactions is approximately

$$\begin{aligned} \dot{S}(3\alpha) &= 5.1 \times 10^8 \rho^2 \left(\frac{X(^4\text{He})}{T_9} \right)^3 \\ &\quad \times \exp \left(-\frac{4.4027}{T_9} \right) \text{ ergs g}^{-1} \text{ s}^{-1}, \\ \dot{S}[^{12}\text{C}(\alpha\gamma)] &= \frac{1.5 \times 10^{25} X(^4\text{He})X(^{12}\text{C})\rho}{T_9^2} \\ &\quad \times (1.0 + 0.0489 T_9^{-2/3})^{-2} \\ &\quad \times \exp(-32.12 T_9^{-1/3} - 0.0818 T_9^2) \\ &\quad \times \text{ergs g}^{-1} \text{ s}^{-1}, \end{aligned} \quad (7)$$

where $T_9 = T/10^9$ (see, for example, Hansen & Kawaler 1994). For any given temperature and composition, there is a density at which the energy generated by these two reactions are equal. Energy liberated by the triple- α reaction dominates below this density, and energy liberated by the $^{12}\text{C}(\alpha, \gamma)^{16}\text{O}$ reaction dominates above this density. The critical temperature, where heating from nuclear reaction rates balances the cooling due to thermal transport, is about $1.7 \times 10^9 \text{ K}$. At this temperature, the two approximate expressions in equation (7) are equal at a density of $\sim 7.8 \times 10^6$, which is very close to the confluence point of Figure 6. Using more exact expressions for the two energy generation rates gives a density that coincides almost exactly with the confluence point.

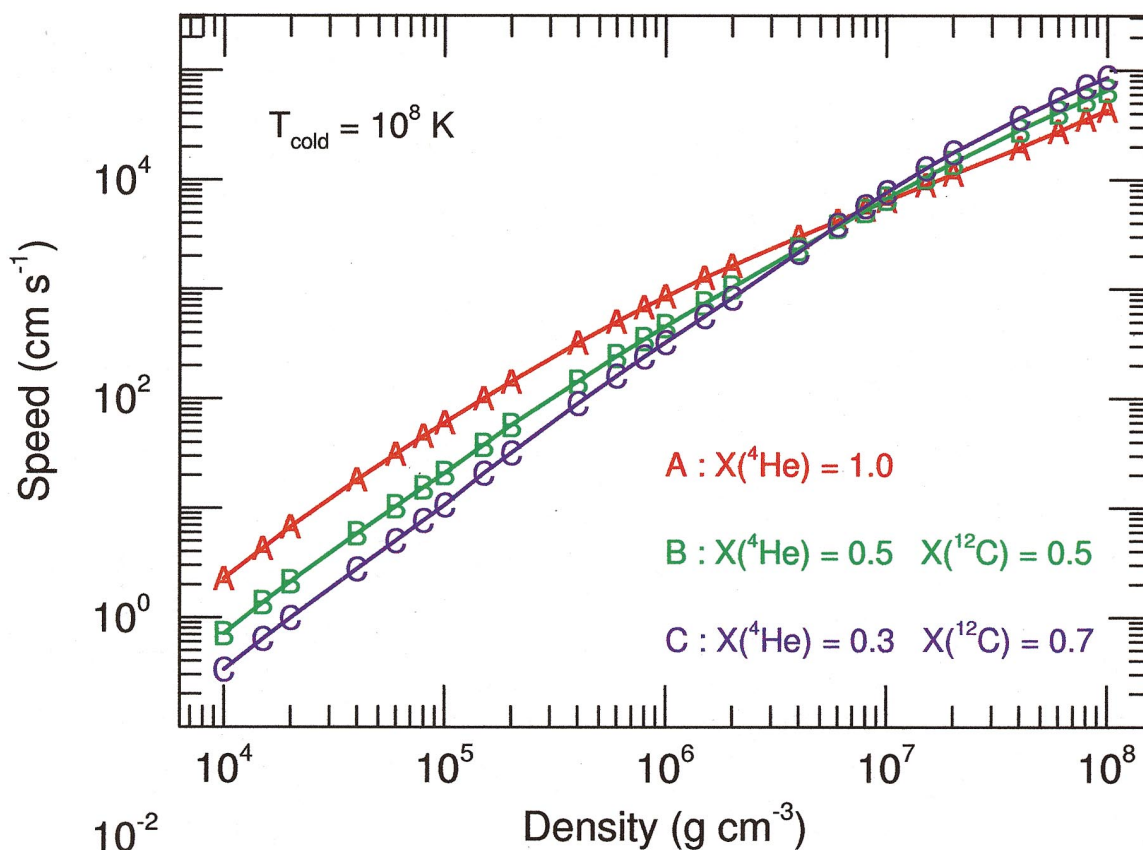


FIG. 6.—Steady state deflagration speeds for the pure helium, half-helium-half-carbon, and 30% helium-70% carbon compositions at an upstream temperature of 10^8 K. Upstream densities are shown on the x-axis and the deflagration speed on the y-axis. Each colored curve corresponds to a different composition. Adding carbon to the upstream material decreases the flame speed because the energy generation rate is suppressed.

Hence, the confluence point of Figure 6 results from equality of the contributions to the energy generation rate from the triple- α and $^{12}\text{C}(\alpha, \gamma)^{16}\text{O}$ reactions. Energy released from the triple- α reaction dominates at densities smaller than the density at the confluence point. In this region the energy generation rate is $\dot{S} \propto X(^4\text{He})^3$. Reducing the helium abundance in the upstream composition reduces the energy generation rate, which reduces the flame speed. This explains the composition dependence of the flame speeds below the confluence point. Energy liberated by the $^{12}\text{C}(\alpha, \gamma)^{16}\text{O}$ reaction dominates at densities above the density at the confluence point. In this region the energy generation rate is $\dot{S} \propto X(^4\text{He})X(^{12}\text{C})$. Increasing the carbon abundance increases the contribution from the $^{12}\text{C}(\alpha, \gamma)^{16}\text{O}$ and decreases contributions from the triple- α reaction. This explains the composition dependence of the flame speeds at densities above the confluence point in Figure 6.

Previous studies of laminar helium deflagrations were reported by Bildsten (1995), whose primary focus was on the thermodynamic conditions that occur in the helium-carbon layer of accreting neutron stars. As such, Bildsten reported laminar deflagration speeds for a single $X(^4\text{He})=0.33$, $X(^{12}\text{C})=0.67$ composition and a single upstream temperature of 3×10^8 K. Bildsten also employed a 2 isotope reaction network which converted helium to carbon by the triple- α reaction.

Figure 7 shows a comparison of the laminar flame speeds given by Bildsten (1995) and the laminar speeds calculated in this survey. The isobaric pressure is given on the x-axis, and the deflagration speed is given on the y-axis. Green “B”

symbols correspond to the helium deflagration speeds given by Bildsten (1995). The blue curve shows the flame speeds when the same 2 isotope reaction network that Bildsten employed is used. The agreement with Bildsten’s results are quite reasonable given the small differences that exist in the upstream composition [$X(^4\text{He})=0.33$ versus $X(^4\text{He})=0.30$], equation of state, and thermal-transport coefficients. The red curve shows the flame speeds when a 3 isotope network, which converts helium to carbon and oxygen by the triple- α and $^{12}\text{C}(\alpha, \gamma)^{16}\text{O}$ reactions, is used. The speeds given by the red curve are faster than the speeds given by the blue curve, by about a factor of 2 at the largest pressures. This is due to the larger energy generation rate within the flame’s reactive width when the $^{12}\text{C}(\alpha, \gamma)^{16}\text{O}$ reaction is allowed to operate. The gray curve shows the flame speeds when the 19 isotope network is used. These flame speeds are only slightly faster than the flame speeds given by the 3 isotope network, which implies that the two helium-burning reactions are the most crucial reactions. Figure 7 indicates that the flame speeds calculated by Bildsten (1995) agree with the flame speeds calculated in this survey when helium is only allowed to be processed into carbon. When helium is permitted to be processed into at least carbon and oxygen by including the $^{12}\text{C}(\alpha, \gamma)^{16}\text{O}$ reaction, the calculated flame speeds are faster than the flame speeds reported by Bildsten (1995).

The sensitivity of the flame speed to the nuclear reaction network used was examined by using the five different networks discussed in § 2.3. The results, given in Figure 7, indicate that the use of a small network will underestimate

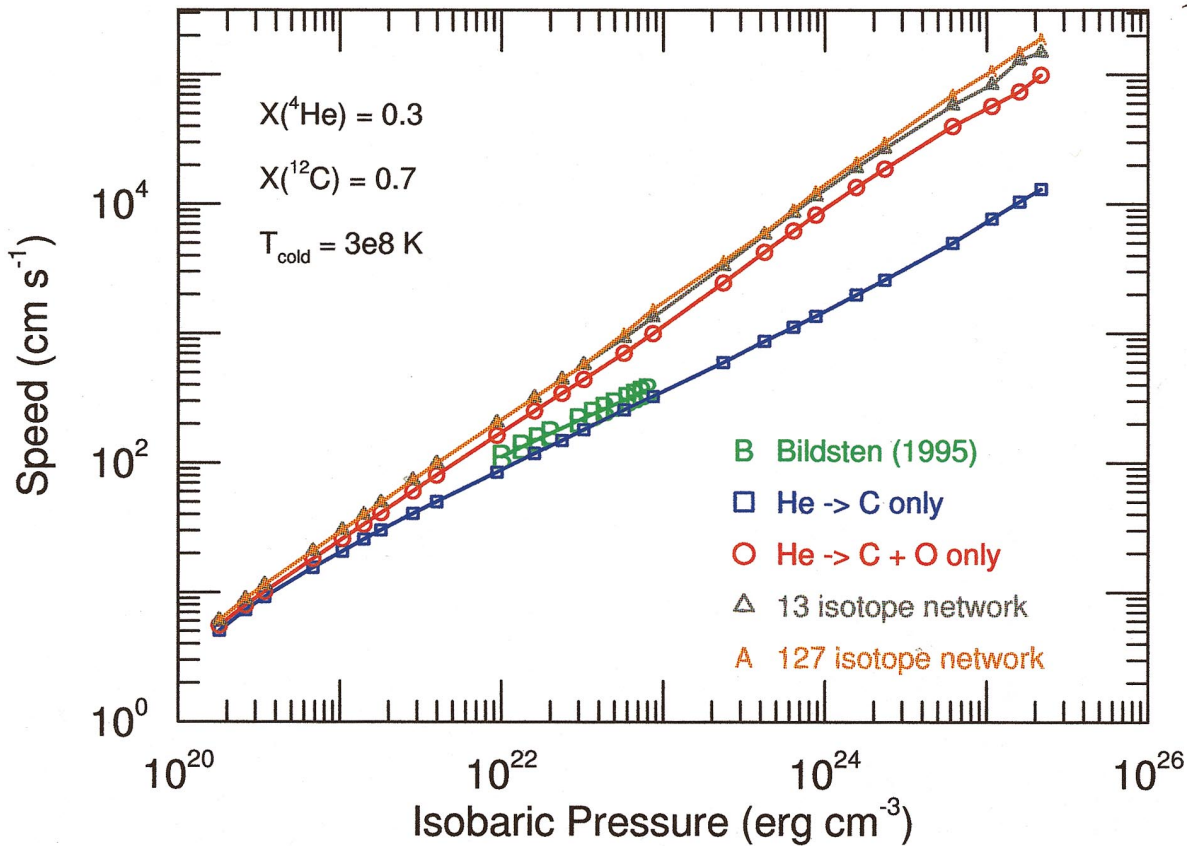


FIG. 7.—Steady state deflagration speeds for different reaction networks. The x-axis shows the isobaric pressure, while the y-axis shows the deflagration speeds for an upstream temperature of 3×10^8 . The green “B” symbols correspond to the helium deflagration speeds given by Bildsten (1995), who used a 2 isotope reaction network that converted helium to carbon by the triple- α reaction. Flame speeds calculated here for the same reaction network used by Bildsten are shown by the blue curve. The agreement with Bildsten’s results is quite reasonable. The red curve shows the flame speeds when helium is permitted to burn to carbon and oxygen. These flame speeds are larger, by about a factor of 2 at the largest pressures, because the energy generation rate within the flame’s reactive width is larger. Flame speeds calculated with the 13 isotope network are shown as the gray curve, and are only slightly faster than the flame speeds calculated with the 3 isotope network (red curve).

the flame speed. The flattening of the flame speed with increasing number of isotopes is expected as the nuclear energy generation rate becomes well defined at a modest number of isotopes, approaching the correct value asymptotically.

The effects of changing the triple- α , $^{12}\text{C}(\alpha, \gamma)^{16}\text{O}$, $^{16}\text{O}(\alpha, \gamma)^{20}\text{Ne}$, and $^{20}\text{Ne}(\alpha, \gamma)^{24}\text{Mg}$ reaction rates by factors of 0.1, 0.5, 2.0, and 10.0 with the 19 isotope reaction network were investigated. Both the forward and reverse rates were varied by the same factor in order to preserve detailed balance. Not surprisingly, the largest changes in the flame speed were due to variations in the helium-burning reactions. Variations in the other reaction rates made no significant changes to the properties of the helium deflagrations. The scaling relation between the flame speed and the energy generation rate are predicted rather well by the order-of-magnitude estimate given in equation (6), i.e., increasing the $^{12}\text{C}(\alpha, \gamma)^{16}\text{O}$ by 10.0 results in flame speeds that are faster by about a factor of 3.

The response of the helium deflagration flame speeds to variations in the thermal transport coefficients discussed in § 2.2 and the Appendix was analyzed by multiplying the radiative and conductive contributions by factors of 0.1, 0.5, 2.0, and 10.0. The scaling relation between the flame speed and the thermal-transport coefficient are predicted rather well by the order-of-magnitude estimate given in equation (6), i.e., increasing the total opacity by 10.0 results in flame

speeds that are slower by about a factor of 3. The flame speed is more sensitive to the energy transport coefficients than to the number of isotopes in the nuclear reaction network.

The sensitivity of the flame speeds to using the different equations of state was assessed by running several dozen helium deflagrations with the six different equations of state discussed in § 2.1. The primary role of the equation of state in helium deflagrations is to set and enforce the isobaric condition (determined from the upstream density, temperature, and composition). The pressures and specific thermal energies calculated by each equation-of-state routine typically differ by 0.1% or less, despite the different approaches and approximations used in each routine. The derivatives of the pressure and specific thermal energies with respect to the temperature and density typically differ by 1% or less. As a result of this level of agreement, the helium deflagration flame speeds calculated by using different equation-of-state routines varied by only a fraction of a percent.

Failure to include the $P dV$ work term in the reaction-diffusion equations artificially elevates the temperature. This increases the corresponding nuclear energy generation rate, and hence, by equation (6), increases the flame speed. Allowing the $P dV$ work term to operate allows a region to expand. The increased volume dilutes the thermal energy density which decreases the temperature. The energy-

generation rate is then suppressed, and the flame speed correspondingly decreases. Several runs were done with the $P dV$ work term turned off, and the resulting flame speeds were about 25% larger than the flame speeds when the $P dV$ work term was allowed to operate.

Tables 2–22 detail the physical properties of helium deflagrations, which were calculated for the 127 isotope reaction network, the Helmholtz equation of state, and the thermal transport coefficient routine listed in the Appendix. They are the main pragmatic result of this survey. Interpolation in the tables is the preferred method for incorporating the physical properties of laminar helium deflagrations into flame-tracking algorithms (e.g., Arnett & Livne 1994; Oran & Boris 1987), or into subgrid models, for hydrodynamic programs. There may be occasions when a simple fitting formula of modest accuracy for the most important property—the flame speed—is desirable. Substituting equation (7) for the nuclear energy generation rates and power expansions for the specific thermal energy E and opacity κ into the order-of-magnitude estimate in equation (6) leads to the rough fitting formula

$$V_{\text{cond}} \sim 8.5 \times 10^2 \left(\frac{\rho}{10^6} \right)^{1.07} \left(\frac{T}{10^8} \right)^{0.303} \times X(^4\text{He})^{0.899} \text{ cm s}^{-1}, \quad (8)$$

where the density, temperature, and helium mass fraction are the upstream values. While this fitting formula reproduces the flame-speed trends, it must be stressed that the fitting formula is only accurate in absolute terms to about a factor of 3. Caution is advised in interpreting hydrodynamic models that rely on equation (8) for critical analysis.

3.1. Critical Temperatures

The left-hand side of the first expression in equation (4) is zero in the steady state:

$$\frac{d}{dx} \left(\sigma \frac{dT}{dx} \right) = \rho \dot{S}. \quad (9)$$

The temperature along the flame front where this expression is exactly satisfied is an important diagnostic, and is referred to as the critical temperature, T_{crit} . At the critical temperature, the energy generation rate equals the energy conduction term (heating equals cooling). Regions upstream of the critical temperature are dominated by the cooling effect of thermal conduction, while regions downstream are dominated by the heating effect of energy released from nuclear reactions. Any laminar deflagration that is to achieve steady state propagation must be capable of achieving the critical temperature.

The competition between energy generation and energy transport is shown in Figure 8. The x -axis gives the distance, the left y -axis gives the energy rates, and the right y -axis gives the temperature. The figure shows a steady state deflagration propagating into pure helium at a density of 10^6 g cm^{-3} and a temperature of 10^8 K . The red curve shows the temperature profile of the deflagration, with the open circles indicating the grid points. The green curve shows the nuclear energy generation rate, labeled “heating,” while the purple curve shows the thermal energy transport rate, labeled “cooling.” The spike in the thermal energy transport curve arises from the temperature gradient moving into the upstream material. These heating and cooling curves intersect, as indicated by the black arrows, at a distance of $1.02 \times 10^4 \text{ cm}$. The temperature at this dis-

TABLE 2
 $X(^4\text{He} = 1.0)$, $T_{\text{upstream}} = 3.0 \times 10^8 \text{ K}$

Density (g cm^{-3})	Speed (cm s^{-1})	Thermal Width (cm)	Reaction Width (cm)	$\Delta\rho/\rho$	T_{crit} (K)	P_{isobaric} (ergs cm^{-3})
1.0E+08.....	7.537E+04	4.787E-02	4.350E-02	3.133E-01	3.089E+09	2.216E+25
8.0E+07.....	6.333E+04	9.390E-01	5.884E-02	4.454E-01	3.009E+09	1.636E+25
6.0E+07.....	5.026E+04	1.474E+00	9.115E-02	4.763E-01	2.877E+09	1.104E+25
4.0E+07.....	3.641E+04	2.045E-01	1.725E-01	4.032E-01	2.713E+09	6.329E+24
2.0E+07.....	2.165E+04	5.962E-01	5.009E-01	4.752E-01	2.458E+09	2.423E+24
1.5E+07.....	1.702E+04	1.024E+00	8.265E-01	5.043E-01	2.330E+09	1.621E+24
1.0E+07.....	1.219E+04	3.673E+00	1.733E+00	6.131E-01	2.159E+09	9.170E+23
8.0E+06.....	1.016E+04	3.240E+00	2.726E+00	5.752E-01	2.083E+09	6.692E+23
6.0E+06.....	7.866E+03	1.172E+01	4.713E+00	6.827E-01	1.968E+09	4.451E+23
4.0E+06.....	5.517E+03	1.656E+01	1.040E+01	6.801E-01	1.809E+09	2.502E+23
2.0E+06.....	2.975E+03	4.449E+01	5.171E+01	7.008E-01	1.531E+09	9.360E+22
1.5E+06.....	2.231E+03	8.561E+01	1.046E+02	7.306E-01	1.371E+09	6.260E+22
1.0E+06.....	1.518E+03	2.122E+02	2.715E+02	7.475E-01	8.533E+08	3.569E+22
8.0E+05.....	1.247E+03	3.337E+02	4.286E+02	7.541E-01	7.914E+08	2.637E+22
6.0E+05.....	9.637E+02	5.960E+02	7.684E+02	7.597E-01	7.198E+08	1.800E+22
4.0E+05.....	6.742E+02	1.333E+03	1.848E+03	7.679E-01	6.421E+08	1.069E+22
2.0E+05.....	3.779E+02	6.479E+03	8.464E+02	7.861E-01	5.492E+08	4.614E+21
1.5E+05.....	3.000E+02	1.189E+04	1.647E+03	7.897E-01	5.191E+08	3.315E+21
1.0E+05.....	2.185E+02	3.083E+04	4.018E+03	8.000E-01	4.808E+08	2.112E+21
8.0E+04.....	1.832E+02	4.559E+04	6.167E+03	7.986E-01	4.623E+08	1.660E+21
6.0E+04.....	1.456E+02	7.747E+04	1.165E+04	7.786E-01	4.403E+08	1.224E+21
4.0E+04.....	1.047E+02	1.533E+05	2.700E+04	7.682E-01	4.111E+08	8.050E+20
2.0E+04.....	5.886E+01	5.061E+05	1.099E+05	7.238E-01	3.633E+08	4.037E+20
1.5E+04.....	4.577E+01	7.494E+05	1.999E+05	6.871E-01	3.427E+08	3.062E+20
1.0E+04.....	3.098E+01	1.506E+06	4.055E+05	6.603E-01	3.244E+08	2.098E+20

TABLE 3
 $X(^4\text{He} = 1.0)$, $T_{\text{upstream}} = 2.0 \times 10^8$ K

Density (g cm^{-3})	Speed (cm s^{-1})	Thermal Width (cm)	Reaction Width (cm)	$\Delta\rho/\rho$	T_{crit} (K)	P_{isobaric} (ergs cm^{-3})
1.0E+08.....	7.141E+04	4.596E-02	4.313E-02	3.160E-01	3.067E+09	2.194E+25
8.0E+07.....	5.966E+04	1.156E+00	6.149E-02	4.427E-01	2.973E+09	1.618E+25
6.0E+07.....	4.747E+04	1.657E+00	9.302E-02	4.757E-01	2.849E+09	1.090E+25
4.0E+07.....	3.510E+04	1.996E-01	1.685E-01	4.132E-01	2.710E+09	6.235E+24
2.0E+07.....	2.077E+04	6.116E-01	5.142E-01	4.880E-01	2.449E+09	2.375E+24
1.5E+07.....	1.631E+04	1.041E+00	8.545E-01	5.150E-01	2.325E+09	1.584E+24
1.0E+07.....	1.163E+04	3.487E+00	1.829E+00	6.116E-01	2.151E+09	8.914E+23
8.0E+06.....	9.679E+03	3.138E+00	2.782E+00	5.785E-01	2.077E+09	6.482E+23
6.0E+06.....	7.430E+03	1.107E+01	4.914E+00	6.735E-01	1.973E+09	4.289E+23
4.0E+06.....	5.214E+03	1.581E+01	1.100E+01	6.829E-01	1.799E+09	2.387E+23
2.0E+06.....	2.757E+03	4.439E+01	5.431E+01	7.193E-01	1.530E+09	8.710E+22
1.5E+06.....	2.030E+03	9.233E+01	1.063E+02	7.411E-01	1.346E+09	5.731E+22
1.0E+06.....	1.337E+03	2.315E+02	2.777E+02	7.723E-01	8.275E+08	3.188E+22
8.0E+05.....	1.059E+03	3.688E+02	5.185E+02	7.821E-01	7.823E+08	2.316E+22
6.0E+05.....	7.963E+02	5.926E+02	9.355E+02	7.764E-01	7.115E+08	1.542E+22
4.0E+05.....	5.248E+02	1.567E+03	2.247E+02	8.045E-01	6.287E+08	8.809E+21
2.0E+05.....	2.570E+02	5.917E+03	1.160E+03	8.027E-01	5.311E+08	3.547E+21
1.5E+05.....	1.916E+02	1.380E+04	2.296E+03	8.189E-01	4.979E+08	2.481E+21
1.0E+05.....	1.278E+02	4.179E+04	5.871E+03	8.587E-01	4.575E+08	1.528E+21
8.0E+04.....	1.019E+02	6.411E+04	9.929E+03	8.371E-01	4.384E+08	1.181E+21
6.0E+04.....	7.592E+01	1.102E+05	1.920E+04	8.346E-01	4.160E+08	8.546E+20
4.0E+04.....	4.983E+01	2.103E+05	4.855E+04	8.234E-01	3.872E+08	5.489E+20
2.0E+04.....	2.330E+01	5.669E+05	2.468E+05	7.589E-01	3.434E+08	2.651E+20
1.5E+04.....	1.668E+01	9.059E+05	4.841E+05	7.316E-01	3.269E+08	1.977E+20
1.0E+04.....	1.018E+01	1.931E+06	1.245E+06	7.007E-01	3.049E+08	1.317E+20

TABLE 4
 $X(^4\text{He} = 1.0)$, $T_{\text{upstream}} = 1.5 \times 10^8$ K

Density (g cm^{-3})	Speed (cm s^{-1})	Thermal Width (cm)	Reaction Width (cm)	$\Delta\rho/\rho$	T_{crit} (K)	P_{isobaric} (ergs cm^{-3})
1.0E+08.....	7.004E+04	5.856E-02	4.327E-02	3.469E-01	3.106E+09	2.183E+25
8.0E+07.....	5.850E+04	8.298E-01	6.052E-02	4.384E-01	2.971E+09	1.609E+25
6.0E+07.....	4.688E+04	1.199E+00	9.470E-02	4.711E-01	2.861E+09	1.084E+25
4.0E+07.....	3.532E+04	1.855E-01	1.744E-01	4.091E-01	2.737E+09	6.190E+24
2.0E+07.....	2.028E+04	6.122E-01	5.255E-01	4.895E-01	2.446E+09	2.352E+24
1.5E+07.....	1.607E+04	1.017E+00	8.475E-01	5.197E-01	2.330E+09	1.567E+24
1.0E+07.....	1.132E+04	3.327E+00	1.853E+00	6.090E-01	2.145E+09	8.794E+23
8.0E+06.....	9.464E+03	3.147E+00	2.758E+00	5.904E-01	2.084E+09	6.384E+23
6.0E+06.....	7.309E+03	1.111E+01	4.825E+00	6.729E-01	1.942E+09	4.213E+23
4.0E+06.....	5.052E+03	1.595E+01	1.193E+01	7.050E-01	1.792E+09	2.334E+23
2.0E+06.....	2.711E+03	3.929E+01	5.277E+01	7.203E-01	1.547E+09	8.419E+22
1.5E+06.....	1.949E+03	9.091E+01	1.144E+02	7.550E-01	1.305E+09	5.501E+22
1.0E+06.....	1.250E+03	2.162E+02	3.286E+02	7.764E-01	8.533E+08	3.022E+22
8.0E+05.....	9.190E+02	3.492E+02	5.481E+02	7.897E-01	1.107E+09	2.176E+22
6.0E+05.....	7.308E+02	6.942E+02	1.109E+03	8.020E-01	7.018E+08	1.429E+22
4.0E+05.....	4.660E+02	1.255E+03	2.509E+02	7.801E-01	6.213E+08	7.978E+21
2.0E+05.....	2.114E+02	7.160E+03	1.405E+03	8.329E-01	5.174E+08	3.063E+21
1.5E+05.....	1.521E+02	1.486E+04	2.897E+03	8.422E-01	4.834E+08	2.098E+21
1.0E+05.....	9.582E+01	5.332E+04	8.054E+03	8.664E-01	4.417E+08	1.257E+21
8.0E+04.....	7.405E+01	8.223E+04	1.373E+04	8.690E-01	4.221E+08	9.577E+20
6.0E+04.....	5.297E+01	1.348E+05	2.712E+04	8.485E-01	3.989E+08	6.815E+20
4.0E+04.....	3.283E+01	2.556E+05	7.247E+04	8.396E-01	3.696E+08	4.292E+20
2.0E+04.....	1.389E+01	6.906E+05	3.927E+05	7.851E-01	3.263E+08	2.020E+20
1.5E+04.....	9.468E+01	1.215E+06	8.006E+05	7.744E-01	3.103E+08	1.493E+20
1.0E+04.....	5.374E+00	3.110E+06	2.266E+06	7.646E-01	2.887E+08	9.827E+19

TABLE 5

 $X(^4\text{He} = 1.0)$, $T_{\text{upstream}} = 1.0 \times 10^8$ K

Density (g cm^{-3})	Speed (cm s^{-1})	Thermal Width (cm)	Reaction Width (cm)	$\Delta\rho/\rho$	T_{crit} (K)	P_{isobaric} (ergs cm^{-3})
1.0E+08.....	6.844E+04	4.530E-02	4.459E-02	3.231E-01	3.068E+09	2.172E+25
8.0E+07.....	5.743E+04	1.070E+00	5.929E-02	4.456E-01	2.972E+09	1.600E+25
6.0E+07.....	4.610E+04	1.616E+00	9.577E-02	4.772E-01	2.852E+09	1.077E+25
4.0E+07.....	3.497E+04	1.880E-01	1.652E-01	4.195E-01	2.750E+09	6.146E+24
2.0E+07.....	2.016E+04	6.001E-01	5.031E-01	4.976E-01	2.460E+09	2.329E+24
1.5E+07.....	1.591E+04	9.922E-01	8.174E-01	5.278E-01	2.337E+09	1.549E+24
1.0E+07.....	1.109E+04	3.189E+00	1.831E+00	6.106E-01	2.141E+09	8.678E+23
8.0E+06.....	9.296E+03	3.094E+00	2.748E+00	5.916E-01	2.080E+09	6.290E+23
6.0E+06.....	7.117E+03	1.021E+01	4.820E+00	7.248E-01	1.975E+09	4.141E+23
4.0E+06.....	4.915E+03	1.513E+01	1.219E+01	7.024E-01	1.788E+09	2.285E+23
2.0E+06.....	2.618E+03	3.240E+01	4.739E+01	6.695E-01	1.502E+09	8.151E+22
1.5E+06.....	1.955E+03	9.857E+01	1.364E+02	7.584E-01	1.219E+09	5.292E+22
1.0E+06.....	1.166E+03	1.609E+02	2.548E+02	7.401E-01	8.952E+08	2.872E+22
8.0E+05.....	9.419E+02	2.764E+02	4.547E+02	7.649E-01	7.826E+08	2.051E+22
6.0E+05.....	6.633E+02	7.095E+02	1.698E+03	8.007E-01	6.847E+08	1.330E+22
4.0E+05.....	4.101E+02	2.146E+03	2.811E+02	8.446E-01	6.077E+08	7.247E+21
2.0E+05.....	1.771E+02	5.995E+03	1.710E+03	8.232E-01	5.075E+08	2.630E+21
1.5E+05.....	1.200E+02	1.620E+04	3.730E+03	8.505E-01	4.687E+08	1.751E+21
1.0E+05.....	7.001E+01	6.948E+04	1.115E+04	8.814E-01	4.237E+08	1.006E+21
8.0E+04.....	5.182E+01	1.006E+05	1.986E+04	8.733E-01	4.038E+08	7.498E+20
6.0E+04.....	3.486E+01	1.607E+05	4.262E+04	8.760E-01	3.793E+08	5.190E+20
4.0E+04.....	2.007E+01	2.716E+05	1.234E+05	8.510E-01	3.494E+08	3.157E+20
2.0E+04.....	7.338E+00	1.181E+06	7.814E+05	8.320E-01	3.052E+08	1.419E+20
1.5E+04.....	4.694E+00	3.053E+06	1.714E+06	8.498E-01	2.889E+08	1.034E+20
1.0E+04.....	2.458E+00	6.074E+06	5.078E+06	8.205E-01	2.685E+08	6.692E+19

TABLE 6

 $X(^4\text{He} = 1.0)$, $T_{\text{upstream}} = 8.0 \times 10^7$ K

Density (g cm^{-3})	Speed (cm s^{-1})	Thermal Width (cm)	Reaction Width (cm)	$\Delta\rho/\rho$	T_{crit} (K)	P_{isobaric} (ergs cm^{-3})
1.0E+08.....	6.789E+04	4.508E-02	4.349E-02	3.231E-01	3.068E+09	2.168E+25
8.0E+07.....	5.710E+04	1.108E+00	6.004E-02	4.439E-01	2.962E+09	1.597E+25
6.0E+07.....	4.568E+04	1.646E+00	9.265E-02	4.745E-01	2.854E+09	1.075E+25
4.0E+07.....	3.492E+04	1.851E-01	1.625E-01	4.215E-01	2.758E+09	6.129E+24
2.0E+07.....	2.011E+04	5.829E-01	4.978E-01	4.945E-01	2.469E+09	2.320E+24
1.5E+07.....	1.594E+04	9.529E-01	7.952E-01	5.381E-01	2.348E+09	1.543E+24
1.0E+07.....	1.106E+04	3.112E+00	1.777E+00	6.109E-01	2.143E+09	8.632E+23
8.0E+06.....	9.310E+03	3.029E+00	2.748E+00	5.997E-01	2.093E+09	6.253E+23
6.0E+06.....	7.099E+03	1.049E+01	5.136E+00	7.217E-01	1.952E+09	4.113E+23
4.0E+06.....	4.903E+03	1.482E+01	1.135E+01	7.012E-01	1.792E+09	2.266E+23
2.0E+06.....	2.465E+03	3.262E+01	4.490E+01	6.748E-01	1.443E+09	8.051E+22
1.5E+06.....	1.820E+03	6.074E+01	9.453E+01	6.963E-01	1.259E+09	5.214E+22
1.0E+06.....	9.064E+02	1.213E+02	1.945E+02	6.972E-01	8.103E+08	2.817E+22
8.0E+05.....	9.042E+02	2.983E+02	4.516E+02	7.792E-01	7.786E+08	2.006E+22
6.0E+05.....	6.316E+02	5.095E+02	4.899E+03	7.679E-01	6.802E+08	1.294E+22
4.0E+05.....	4.018E+02	1.250E+03	2.830E+02	8.079E-01	6.090E+08	6.987E+21
2.0E+05.....	1.647E+02	6.416E+03	1.851E+03	8.386E-01	5.017E+08	2.476E+21
1.5E+05.....	1.096E+02	1.727E+04	4.092E+03	8.485E-01	4.621E+08	1.627E+21
1.0E+05.....	6.152E+01	7.714E+04	1.278E+04	8.983E-01	4.175E+08	9.156E+20
8.0E+04.....	4.433E+01	1.118E+05	2.352E+04	8.933E-01	3.957E+08	6.736E+20
6.0E+04.....	2.913E+01	1.701E+05	5.209E+04	8.767E-01	3.712E+08	4.586E+20
4.0E+04.....	1.595E+01	2.988E+05	1.671E+05	8.571E-01	3.403E+08	2.728E+20
2.0E+04.....	5.222E+00	2.279E+06	1.126E+06	8.775E-01	2.939E+08	1.188E+20
1.5E+04.....	3.265E+00	4.558E+06	2.513E+06	8.801E-01	2.788E+08	8.571E+19
1.0E+04.....	1.634E+00	9.759E+06	8.070E+06	8.494E-01	2.582E+08	5.482E+19

TABLE 7
 $X(^4\text{He} = 1.0)$, $T_{\text{upstream}} = 6.0 \times 10^7$ K

Density (g cm^{-3})	Speed (cm s^{-1})	Thermal Width (cm)	Reaction Width (cm)	$\Delta\rho/\rho$	T_{crit} (K)	P_{isobaric} (ergs cm^{-3})
1.0E+08.....	6.735E+04	4.652E-02	4.137E-02	3.303E-01	3.081E+09	2.163E+25
8.0E+07.....	5.654E+04	1.122E+00	5.954E-02	4.419E-01	2.954E+09	1.593E+25
6.0E+07.....	4.511E+04	1.598E+00	9.230E-02	4.742E-01	2.844E+09	1.072E+25
4.0E+07.....	3.502E+04	1.809E-01	1.664E-01	4.330E-01	2.769E+09	6.112E+24
2.0E+07.....	2.028E+04	5.692E-01	5.028E-01	5.069E-01	2.481E+09	2.312E+24
1.5E+07.....	1.615E+04	9.054E-01	8.484E-01	5.326E-01	2.367E+09	1.536E+24
1.0E+07.....	1.097E+04	2.931E+00	1.743E+00	6.062E-01	2.167E+09	8.588E+23
8.0E+06.....	9.356E+03	2.916E+00	2.721E+00	5.964E-01	2.093E+09	6.217E+23
6.0E+06.....	7.075E+03	1.052E+01	4.636E+00	7.162E-01	1.957E+09	4.086E+23
4.0E+06.....	4.893E+03	1.408E+01	1.161E+01	6.950E-01	1.801E+09	2.247E+23
2.0E+06.....	1.813E+03	1.789E+01	7.197E+00	5.377E-01	8.273E+08	7.954E+22
1.5E+06.....	1.776E+03	6.113E+01	9.187E+01	7.114E-01	1.173E+09	5.140E+22
1.0E+06.....	1.206E+03	1.564E+02	2.282E+02	7.358E-01	8.197E+08	2.765E+22
8.0E+05.....	8.697E+02	2.432E+02	3.529E+02	7.421E-01	7.519E+08	1.963E+22
6.0E+05.....	6.051E+02	3.122E+02	1.020E+02	7.192E-01	6.698E+08	1.260E+22
4.0E+05.....	3.771E+02	7.492E+02	2.994E+02	7.547E-01	5.969E+08	6.746E+21
2.0E+05.....	1.503E+02	6.880E+03	1.988E+03	8.323E-01	4.934E+08	2.336E+21
1.5E+05.....	9.975E+01	1.831E+04	4.494E+03	8.691E-01	4.560E+08	1.515E+21
1.0E+05.....	5.449E+01	3.607E+04	1.501E+04	8.527E-01	4.109E+08	8.326E+20
8.0E+04.....	3.842E+01	7.778E+04	2.810E+04	8.727E-01	3.888E+08	6.035E+20
6.0E+04.....	2.393E+01	1.575E+05	6.548E+04	8.720E-01	3.617E+08	4.026E+20
4.0E+04.....	1.208E+01	7.152E+05	2.191E+05	9.062E-01	3.287E+08	2.324E+20
2.0E+04.....	3.566E+00	2.824E+06	1.715E+06	8.852E-01	2.828E+08	9.660E+19
1.5E+04.....	2.108E+00	5.832E+06	4.117E+06	8.819E-01	2.664E+08	6.855E+19
1.0E+04.....	9.712E-01	1.727E+07	1.434E+07	8.778E-01	2.454E+08	4.303E+19

TABLE 8
 $X(^4\text{He} = 1.0)$, $T_{\text{upstream}} = 4.0 \times 10^7$ K

Density (g cm^{-3})	Speed (cm s^{-1})	Thermal Width (cm)	Reaction Width (cm)	$\Delta\rho/\rho$	T_{crit} (K)	P_{isobaric} (ergs cm^{-3})
1.0E+08.....	6.704E+04	5.096E-02	4.171E-02	3.385E-01	3.068E+09	2.159E+25
8.0E+07.....	5.595E+04	2.985E+00	5.932E-02	4.384E-01	2.949E+09	1.590E+25
6.0E+07.....	4.490E+04	3.020E+00	9.230E-02	4.731E-01	2.829E+09	1.070E+25
4.0E+07.....	3.508E+04	1.771E-01	1.606E-01	4.338E-01	2.778E+09	6.095E+24
2.0E+07.....	2.040E+04	5.490E-01	5.076E-01	5.006E-01	2.487E+09	2.303E+24
1.5E+07.....	1.655E+04	8.124E-01	8.354E-01	5.261E-01	2.408E+09	1.530E+24
1.0E+07.....	1.090E+04	2.898E+00	1.767E+00	6.051E-01	2.149E+09	8.545E+23
8.0E+06.....	9.424E+03	2.765E+00	2.694E+00	6.061E-01	2.108E+09	6.182E+23
6.0E+06.....	7.014E+03	1.182E+01	4.976E+00	7.182E-01	1.959E+09	4.060E+23
4.0E+06.....	4.826E+03	1.400E+01	1.097E+01	7.340E-01	1.798E+09	2.230E+23
2.0E+06.....	1.768E+03	1.820E+01	7.100E+00	5.522E-01	8.372E+08	7.861E+22
1.5E+06.....	1.765E+03	6.538E+01	9.489E+01	7.154E-01	1.143E+09	5.069E+22
1.0E+06.....	9.947E+02	8.924E+01	3.072E+01	6.477E-01	7.542E+08	2.716E+22
8.0E+05.....	7.844E+02	1.359E+02	5.248E+01	6.667E-01	7.094E+08	1.923E+22
6.0E+05.....	5.844E+02	3.391E+02	1.029E+02	7.262E-01	6.764E+08	1.229E+22
4.0E+05.....	3.603E+02	9.155E+02	3.047E+02	7.676E-01	5.970E+08	6.527E+21
2.0E+05.....	1.308E+02	1.047E+04	2.206E+03	8.483E-01	4.617E+08	2.212E+21
1.5E+05.....	8.769E+01	1.848E+04	5.042E+03	8.525E-01	4.450E+08	1.415E+21
1.0E+05.....	3.768E+01	2.351E+04	2.591E+04	8.029E-01	3.728E+08	7.594E+20
8.0E+04.....	2.998E+01	6.157E+04	3.915E+04	8.540E-01	3.740E+08	5.417E+20
6.0E+04.....	1.964E+01	2.583E+05	8.228E+04	8.987E-01	3.519E+08	3.527E+20
4.0E+04.....	9.268E+00	6.446E+05	3.041E+05	9.015E-01	3.197E+08	1.959E+20
2.0E+04.....	2.319E+00	4.054E+06	2.996E+06	9.055E-01	2.715E+08	7.580E+19
1.5E+04.....	1.290E+00	8.070E+06	7.448E+06	8.997E-01	2.554E+08	5.231E+19
1.0E+04.....	5.283E-01	2.934E+07	2.768E+07	9.032E-01	2.343E+08	3.172E+19

TABLE 9
 $X(^4\text{He} = 0.5)$, $X(^{12}\text{C} = 0.5)$, $T_{\text{upstream}} = 3.0 \times 10^8 \text{ K}$

Density (g cm^{-3})	Speed (cm s^{-1})	Thermal Width (cm)	Reaction Width (cm)	$\Delta\rho/\rho$	T_{crit} (K)	P_{isobaric} (ergs cm^{-3})
1.0E+08	1.128E+06	4.565E-03	3.444E-03	4.323E-01	4.223E+09	2.196E+25
8.0E+07	9.253E+05	6.402E-03	4.950E-03	4.522E-01	4.107E+09	1.619E+25
6.0E+07	6.969E+05	1.085E-02	8.461E-03	4.838E-01	3.935E+09	1.092E+25
4.0E+07	4.333E+05	2.321E-02	1.924E-02	5.158E-01	3.662E+09	6.245E+24
2.0E+07	1.633E+05	1.003E-01	9.541E-02	5.746E-01	3.185E+09	2.382E+24
1.5E+07	1.031E+05	2.030E-01	2.001E-01	5.973E-01	2.972E+09	1.590E+24
1.0E+07	5.495E+04	5.148E-01	5.564E-01	6.291E-01	2.680E+09	8.963E+23
8.0E+06	4.215E+04	8.262E-01	1.004E+00	6.620E-01	2.561E+09	6.525E+23
6.0E+06	2.558E+04	1.782E+00	1.900E+00	6.776E-01	2.315E+09	4.327E+23
4.0E+06	1.315E+04	4.872E+00	5.584E+00	6.794E-01	2.025E+09	2.419E+23
2.0E+06	4.396E+03	2.771E+01	3.692E+01	7.190E-01	1.603E+09	8.944E+22
1.5E+06	2.808E+03	5.913E+01	7.395E+01	7.263E-01	1.433E+09	5.938E+22
1.0E+06	1.572E+03	1.622E+02	1.971E+02	7.447E-01	1.223E+09	3.361E+22
8.0E+05	1.168E+03	2.763E+02	3.168E+02	7.575E-01	1.128E+09	2.471E+22
6.0E+05	8.141E+02	5.442E+02	6.386E+02	7.609E-01	1.027E+09	1.675E+22
4.0E+05	5.010E+02	1.308E+03	1.429E+03	7.672E-01	9.166E+08	9.857E+21
2.0E+05	2.264E+02	5.575E+03	6.031E+03	7.658E-01	7.581E+08	4.198E+21
1.5E+05	1.634E+02	1.081E+04	1.045E+04	7.696E-01	6.911E+08	3.003E+21
1.0E+05	1.062E+02	2.273E+04	2.722E+04	7.486E-01	5.972E+08	1.904E+21
8.0E+04	8.358E+01	3.764E+04	4.656E+04	7.421E-01	5.301E+08	1.493E+21
6.0E+04	6.167E+01	7.329E+04	9.561E+04	7.382E-01	4.717E+08	1.099E+21
4.0E+04	4.130E+01	1.985E+05	2.621E+05	7.309E-01	4.165E+08	7.218E+20
2.0E+04	2.210E+01	8.428E+05	8.889E+05	6.765E-01	3.524E+08	3.621E+20
1.5E+04	1.705E+01	1.506E+06	1.856E+06	6.530E-01	3.342E+08	2.750E+20
1.0E+04	1.170E+01	3.461E+06	1.044E+06	6.195E-01	3.240E+08	1.890E+20

TABLE 10
 $X(^4\text{He} = 0.5)$, $X(^{12}\text{C} = 0.5)$, $T_{\text{upstream}} = 2.0 \times 10^8 \text{ K}$

Density (g cm^{-3})	Speed (cm s^{-1})	Thermal Width (cm)	Reaction Width (cm)	$\Delta\rho/\rho$	T_{crit} (K)	P_{isobaric} (ergs cm^{-3})
1.0E+08	1.113E+06	4.625E-03	3.475E-03	4.359E-01	4.215E+09	2.180E+25
8.0E+07	9.115E+05	6.478E-03	5.006E-03	4.551E-01	4.100E+09	1.606E+25
6.0E+07	6.855E+05	1.103E-02	8.418E-03	4.879E-01	3.928E+09	1.082E+25
4.0E+07	4.343E+05	2.333E-02	1.917E-02	5.280E-01	3.665E+09	6.180E+24
2.0E+07	1.589E+05	1.002E-01	9.763E-02	5.795E-01	3.175E+09	2.347E+24
1.5E+07	9.985E+04	2.077E-01	2.067E-01	6.041E-01	2.961E+09	1.563E+24
1.0E+07	5.330E+04	5.283E-01	5.702E-01	6.344E-01	2.669E+09	8.776E+23
8.0E+06	4.113E+04	8.332E-01	1.006E+00	6.656E-01	2.554E+09	6.371E+23
6.0E+06	2.485E+04	1.826E+00	2.221E+00	6.824E-01	2.311E+09	4.206E+23
4.0E+06	1.264E+04	4.992E+00	6.445E+00	7.055E-01	2.014E+09	2.332E+23
2.0E+06	4.062E+03	2.959E+01	3.996E+01	7.202E-01	1.581E+09	8.433E+22
1.5E+06	2.552E+03	6.354E+01	8.543E+01	7.460E-01	1.423E+09	5.524E+22
1.0E+06	1.384E+03	1.818E+02	2.283E+02	7.633E-01	1.197E+09	3.050E+22
8.0E+05	1.013E+03	3.219E+02	3.770E+02	7.792E-01	1.095E+09	2.205E+22
6.0E+05	6.827E+02	6.358E+02	7.111E+02	7.874E-01	9.975E+08	1.459E+22
4.0E+05	3.971E+02	1.614E+03	1.701E+03	8.017E-01	8.830E+08	8.254E+21
2.0E+05	1.570E+02	7.724E+03	7.593E+03	8.116E-01	7.081E+08	3.270E+21
1.5E+05	1.081E+02	1.438E+04	1.588E+04	8.097E-01	6.382E+08	2.273E+21
1.0E+05	6.359E+01	3.729E+04	4.550E+04	8.068E-01	5.245E+08	1.390E+21
8.0E+04	4.746E+01	6.305E+04	8.609E+04	8.042E-01	4.799E+08	1.070E+21
6.0E+04	3.261E+01	1.323E+05	1.786E+05	8.042E-01	4.353E+08	7.714E+20
4.0E+04	1.962E+01	3.436E+05	3.071E+05	7.956E-01	3.902E+08	4.935E+20
2.0E+04	8.282E+00	1.590E+06	1.942E+06	7.669E-01	3.359E+08	2.374E+20
1.5E+04	5.731E+00	3.062E+06	1.460E+06	7.525E-01	3.180E+08	1.769E+20
1.0E+04	3.347E+00	7.921E+06	3.537E+06	7.373E-01	2.959E+08	1.178E+20

TABLE 11
 $X(^4\text{He} = 0.5)$, $X(^{12}\text{C} = 0.5)$, $T_{\text{upstream}} = 1.5 \times 10^8 \text{ K}$

Density (g cm^{-3})	Speed (cm s^{-1})	Thermal Width (cm)	Reaction Width (cm)	$\Delta\rho/\rho$	T_{crit} (K)	P_{isobaric} (ergs cm^{-3})
1.0E+08.....	2.959E+05	8.576E-03	7.491E-03	4.601E-01	1.500E+08	2.172E+25
8.0E+07.....	7.957E+05	8.327E-03	6.405E-03	4.604E-01	3.899E+09	1.600E+25
6.0E+07.....	6.781E+05	1.113E-02	8.401E-03	4.887E-01	3.922E+09	1.078E+25
4.0E+07.....	4.321E+05	2.361E-02	1.913E-02	5.307E-01	3.660E+09	6.149E+24
2.0E+07.....	1.572E+05	1.054E-01	9.975E-02	5.830E-01	3.169E+09	2.331E+24
1.5E+07.....	9.842E+04	2.102E-01	2.080E-01	6.052E-01	2.956E+09	1.551E+24
1.0E+07.....	5.205E+04	5.456E-01	5.868E-01	6.378E-01	2.657E+09	8.690E+23
8.0E+06.....	4.056E+04	8.480E-01	9.765E-01	6.916E-01	2.551E+09	6.300E+23
6.0E+06.....	2.443E+04	1.844E+00	2.186E+00	6.780E-01	2.305E+09	4.151E+23
4.0E+06.....	1.246E+04	5.039E+00	6.355E+00	7.051E-01	2.013E+09	2.293E+23
2.0E+06.....	3.998E+03	2.884E+01	3.669E+01	7.246E-01	1.584E+09	8.211E+22
1.5E+06.....	2.466E+03	6.521E+01	8.631E+01	7.485E-01	1.380E+09	5.345E+22
1.0E+06.....	1.316E+03	1.903E+02	2.397E+02	7.719E-01	1.185E+09	2.918E+22
8.0E+05.....	9.447E+02	3.415E+02	4.009E+02	7.884E-01	1.083E+09	2.093E+22
6.0E+05.....	6.286E+02	6.878E+02	8.277E+02	7.959E-01	9.834E+08	1.367E+22
4.0E+05.....	3.524E+02	1.770E+03	1.980E+03	8.104E-01	8.662E+08	7.562E+21
2.0E+05.....	1.311E+02	8.746E+03	9.145E+03	8.266E-01	6.868E+08	2.855E+21
1.5E+05.....	8.493E+01	1.700E+04	1.976E+04	8.265E-01	6.072E+08	1.942E+21
1.0E+05.....	4.941E+01	4.792E+04	6.083E+04	8.312E-01	4.972E+08	1.153E+21
8.0E+04.....	3.580E+01	6.677E+04	1.183E+05	8.163E-01	4.652E+08	8.745E+20
6.0E+04.....	2.280E+01	1.545E+05	2.141E+05	8.206E-01	4.164E+08	6.192E+20
4.0E+04.....	1.278E+01	4.497E+05	4.572E+05	8.210E-01	3.721E+08	3.877E+20
2.0E+04.....	4.806E+00	2.494E+06	1.181E+06	8.075E-01	3.188E+08	1.813E+20
1.5E+04.....	3.137E+00	5.125E+06	2.379E+06	8.006E-01	3.015E+08	1.337E+20
1.0E+04.....	1.699E+00	1.448E+07	7.015E+06	7.936E-01	2.805E+08	8.788E+19

TABLE 12
 $X(^4\text{He} = 0.5)$, $X(^{12}\text{C} = 0.5)$, $T_{\text{upstream}} = 1.0 \times 10^8 \text{ K}$

Density (g cm^{-3})	Speed (cm s^{-1})	Thermal Width (cm)	Reaction Width (cm)	$\Delta\rho/\rho$	T_{crit} (K)	P_{isobaric} (ergs cm^{-3})
1.0E+08.....	1.097E+06	4.618E-03	3.462E-03	4.382E-01	4.211E+09	2.165E+25
8.0E+07.....	8.993E+05	6.513E-03	5.035E-03	4.581E-01	4.095E+09	1.594E+25
6.0E+07.....	6.756E+05	1.107E-02	8.600E-03	4.915E-01	3.930E+09	1.073E+25
4.0E+07.....	4.265E+05	2.366E-02	1.928E-02	5.321E-01	3.656E+09	6.119E+24
2.0E+07.....	1.552E+05	1.047E-01	1.012E-01	5.826E-01	3.167E+09	2.315E+24
1.5E+07.....	1.002E+05	2.053E-01	1.998E-01	6.150E-01	2.971E+09	1.539E+24
1.0E+07.....	5.154E+04	5.435E-01	5.961E-01	6.427E-01	2.655E+09	8.608E+23
8.0E+06.....	4.124E+04	8.302E-01	9.426E-01	6.924E-01	2.567E+09	6.234E+23
6.0E+06.....	2.458E+04	1.822E+00	2.144E+00	6.784E-01	2.311E+09	4.100E+23
4.0E+06.....	1.247E+04	4.982E+00	6.260E+00	7.061E-01	2.015E+09	2.257E+23
2.0E+06.....	4.002E+03	2.816E+01	4.082E+01	7.248E-01	1.586E+09	8.012E+22
1.5E+06.....	2.474E+03	6.178E+01	8.969E+01	7.524E-01	1.412E+09	5.188E+22
1.0E+06.....	1.275E+03	2.038E+02	2.581E+02	7.794E-01	1.187E+09	2.803E+22
8.0E+05.....	8.954E+02	3.607E+02	4.611E+02	7.932E-01	1.074E+09	1.996E+22
6.0E+05.....	5.901E+02	7.138E+02	8.543E+02	8.073E-01	9.746E+08	1.288E+22
4.0E+05.....	3.295E+02	1.764E+03	2.155E+03	8.184E-01	8.615E+08	6.970E+21
2.0E+05.....	1.099E+02	1.050E+04	1.124E+04	8.465E-01	6.625E+08	2.491E+21
1.5E+05.....	6.913E+01	2.327E+04	2.816E+04	8.532E-01	5.661E+08	1.647E+21
1.0E+05.....	3.476E+01	3.203E+04	5.300E+04	7.915E-01	4.678E+08	9.371E+20
8.0E+04.....	2.488E+01	6.345E+04	1.098E+05	8.139E-01	4.365E+08	6.944E+20
6.0E+04.....	1.549E+01	1.628E+05	2.508E+05	8.362E-01	3.969E+08	4.774E+20
4.0E+04.....	8.221E+00	4.077E+05	7.781E+05	8.258E-01	3.570E+08	2.880E+20
2.0E+04.....	2.507E+00	3.340E+06	2.021E+06	8.314E-01	2.988E+08	1.281E+20
1.5E+04.....	1.528E+00	7.117E+06	4.713E+06	8.237E-01	2.803E+08	9.301E+19
1.0E+04.....	7.603E-01	2.283E+07	1.600E+07	8.184E-01	2.580E+08	5.999E+19

TABLE 13
 $X(^4\text{He} = 0.5)$, $X(^{12}\text{C} = 0.5)$, $T_{\text{upstream}} = 8.0 \times 10^7$ K

Density (g cm^{-3})	Speed (cm s^{-1})	Thermal Width (cm)	Reaction Width (cm)	$\Delta\rho/\rho$	T_{crit} (K)	P_{isobaric} (ergs cm^{-3})
1.0E+08.....	1.095E+06	4.610E-03	3.434E-03	4.392E-01	4.211E+09	2.162E+25
8.0E+07.....	8.970E+05	6.536E-03	5.028E-03	4.606E-01	4.092E+09	1.592E+25
6.0E+07.....	6.715E+05	1.043E-02	8.562E-03	5.162E-01	4.003E+09	1.071E+25
4.0E+07.....	4.251E+05	2.370E-02	1.924E-02	5.326E-01	3.654E+09	6.107E+24
2.0E+07.....	1.544E+05	1.052E-01	1.008E-01	5.849E-01	3.162E+09	2.309E+24
1.5E+07.....	9.967E+04	2.062E-01	2.006E-01	6.158E-01	2.969E+09	1.534E+24
1.0E+07.....	5.127E+04	5.451E-01	5.978E-01	6.436E-01	2.652E+09	8.577E+23
8.0E+06.....	4.185E+04	8.202E-01	8.921E-01	6.840E-01	2.574E+09	6.209E+23
6.0E+06.....	2.525E+04	1.780E+00	1.963E+00	7.034E-01	2.329E+09	4.080E+23
4.0E+06.....	1.276E+04	4.802E+00	5.723E+00	6.924E-01	2.029E+09	2.244E+23
2.0E+06.....	4.084E+03	2.492E+01	3.910E+01	7.218E-01	1.606E+09	7.940E+22
1.5E+06.....	2.472E+03	6.129E+01	8.430E+01	7.604E-01	1.413E+09	5.131E+22
1.0E+06.....	1.328E+03	2.058E+02	2.605E+02	7.874E-01	1.126E+09	2.762E+22
8.0E+05.....	9.259E+02	3.496E+02	4.220E+02	7.981E-01	1.079E+09	1.961E+22
6.0E+05.....	5.862E+02	7.290E+02	8.409E+02	8.237E-01	9.761E+08	1.260E+22
4.0E+05.....	3.112E+02	2.083E+03	2.276E+03	8.311E-01	8.471E+08	6.765E+21
2.0E+05.....	1.016E+02	1.263E+04	1.295E+04	8.558E-01	6.438E+08	2.365E+21
1.5E+05.....	6.335E+01	2.233E+04	3.103E+04	8.560E-01	5.732E+08	1.544E+21
1.0E+05.....	2.661E+01	5.985E+04	9.645E+04	8.431E-01	4.363E+08	8.602E+20
8.0E+04.....	1.987E+01	8.377E+04	1.307E+05	8.372E-01	4.157E+08	6.293E+20
6.0E+04.....	1.215E+01	2.127E+05	3.407E+05	8.543E-01	3.804E+08	4.254E+20
4.0E+04.....	6.099E+00	5.336E+05	3.773E+05	8.318E-01	3.411E+08	2.506E+20
2.0E+04.....	1.796E+00	3.880E+06	2.750E+06	8.491E-01	2.885E+08	1.078E+20
1.5E+04.....	1.083E+00	8.540E+06	6.591E+06	8.390E-01	2.715E+08	7.739E+19
1.0E+04.....	5.206E-01	2.588E+07	2.189E+07	8.331E-01	2.503E+08	4.928E+19

TABLE 14
 $X(^4\text{He} = 0.5)$, $X(^{12}\text{C} = 0.5)$, $T_{\text{upstream}} = 6.0 \times 10^7$ K

Density (g cm^{-3})	Speed (cm s^{-1})	Thermal Width (cm)	Reaction Width (cm)	$\Delta\rho/\rho$	T_{crit} (K)	P_{isobaric} (ergs cm^{-3})
1.0E+08.....	1.092E+06	4.555E-03	3.413E-03	4.398E-01	4.210E+09	2.159E+25
8.0E+07.....	8.943E+05	6.537E-03	5.016E-03	4.617E-01	4.088E+09	1.590E+25
6.0E+07.....	6.719E+05	1.109E-02	8.498E-03	4.949E-01	3.927E+09	1.070E+25
4.0E+07.....	4.236E+05	2.375E-02	1.923E-02	5.332E-01	3.653E+09	6.095E+24
2.0E+07.....	1.538E+05	1.054E-01	1.025E-01	5.850E-01	3.163E+09	2.303E+24
1.5E+07.....	9.915E+04	2.071E-01	2.018E-01	6.170E-01	2.967E+09	1.530E+24
1.0E+07.....	5.103E+04	5.475E-01	5.949E-01	6.427E-01	2.650E+09	8.547E+23
8.0E+06.....	4.196E+04	8.190E-01	1.079E+00	6.815E-01	2.578E+09	6.184E+23
6.0E+06.....	2.528E+04	1.785E+00	2.391E+00	6.988E-01	2.329E+09	4.061E+23
4.0E+06.....	1.283E+04	4.775E+00	6.685E+00	7.148E-01	2.034E+09	2.231E+23
2.0E+06.....	4.026E+03	2.454E+01	3.915E+01	7.264E-01	1.601E+09	7.871E+22
1.5E+06.....	2.477E+03	5.082E+01	8.333E+01	7.340E-01	1.428E+09	5.077E+22
1.0E+06.....	1.323E+03	1.293E+02	2.086E+02	7.449E-01	1.204E+09	2.724E+22
8.0E+05.....	9.431E+02	2.502E+02	4.036E+02	7.717E-01	1.107E+09	1.929E+22
6.0E+05.....	5.819E+02	7.128E+02	8.304E+02	8.156E-01	9.737E+08	1.235E+22
4.0E+05.....	3.185E+02	1.858E+03	2.152E+03	8.263E-01	8.674E+08	6.580E+21
2.0E+05.....	1.054E+02	8.818E+03	1.368E+04	8.364E-01	6.541E+08	2.253E+21
1.5E+05.....	6.222E+01	2.190E+04	3.500E+04	8.607E-01	5.777E+08	1.453E+21
1.0E+05.....	1.774E+01	8.716E+04	1.510E+05	8.229E-01	3.906E+08	7.910E+20
8.0E+04.....	1.294E+01	1.518E+05	2.824E+05	8.338E-01	3.716E+08	5.703E+20
6.0E+04.....	7.370E+00	3.255E+05	1.681E+05	8.395E-01	3.420E+08	3.776E+20
4.0E+04.....	4.188E+00	9.046E+05	5.015E+05	8.589E-01	3.190E+08	2.158E+20
2.0E+04.....	1.239E+00	5.356E+06	4.583E+06	8.593E-01	2.777E+08	8.828E+19
1.5E+04.....	6.854E-01	1.153E+07	1.063E+07	8.572E-01	2.594E+08	6.231E+19
1.0E+04.....	3.159E-01	4.561E+07	3.833E+07	8.789E-01	2.396E+08	3.888E+19

TABLE 15
 $X(^4\text{He} = 0.5)$, $X(^{12}\text{C} = 0.5)$, $T_{\text{upstream}} = 4.0 \times 10^7$ K

Density (g cm^{-3})	Speed (cm s^{-1})	Thermal Width (cm)	Reaction Width (cm)	$\Delta\rho/\rho$	T_{crit} (K)	P_{isobaric} (ergs cm^{-3})
1.0E+08.....	1.089E+06	4.512E-03	3.350E-03	4.397E-01	4.207E+09	2.156E+25
8.0E+07.....	8.921E+05	6.520E-03	4.942E-03	4.617E-01	4.091E+09	1.588E+25
6.0E+07.....	6.704E+05	1.107E-02	8.513E-03	4.958E-01	3.923E+09	1.068E+25
4.0E+07.....	4.222E+05	2.372E-02	1.914E-02	5.336E-01	3.651E+09	6.084E+24
2.0E+07.....	1.528E+05	1.050E-01	1.018E-01	5.854E-01	3.162E+09	2.297E+24
1.5E+07.....	9.875E+04	2.075E-01	2.018E-01	6.176E-01	2.966E+09	1.526E+24
1.0E+07.....	5.073E+04	5.501E-01	5.993E-01	6.441E-01	2.648E+09	8.517E+23
8.0E+06.....	4.152E+04	8.240E-01	1.071E+00	6.750E-01	2.578E+09	6.160E+23
6.0E+06.....	2.502E+04	1.803E+00	1.946E+00	7.012E-01	2.324E+09	4.043E+23
4.0E+06.....	1.271E+04	4.831E+00	6.590E+00	7.093E-01	2.031E+09	2.218E+23
2.0E+06.....	3.955E+03	2.436E+01	3.646E+01	7.095E-01	1.596E+09	7.806E+22
1.5E+06.....	2.340E+03	7.686E+01	1.089E+02	7.642E-01	1.377E+09	5.027E+22
1.0E+06.....	1.263E+03	1.312E+02	1.923E+02	7.498E-01	1.187E+09	2.689E+22
8.0E+05.....	9.174E+02	2.227E+02	3.670E+02	7.617E-01	1.095E+09	1.900E+22
6.0E+05.....	5.903E+02	4.530E+02	7.697E+02	7.669E-01	9.853E+08	1.212E+22
4.0E+05.....	3.764E+02	1.217E+03	2.109E+03	7.928E-01	7.255E+08	6.416E+21
2.0E+05.....	8.208E+01	1.607E+04	1.900E+04	8.750E-01	6.005E+08	2.156E+21
1.5E+05.....	3.223E+01	2.353E+04	3.587E+04	8.062E-01	4.434E+08	1.374E+21
1.0E+05.....	1.394E+01	6.364E+04	4.937E+04	7.838E-01	3.661E+08	7.317E+20
8.0E+04.....	8.546E+00	1.015E+05	1.005E+05	8.077E-01	3.481E+08	5.195E+20
6.0E+04.....	4.389E+00	2.503E+05	3.008E+05	7.960E-01	3.109E+08	3.361E+20
4.0E+04.....	2.091E+00	7.202E+05	7.534E+05	8.064E-01	2.861E+08	1.848E+20
2.0E+04.....	4.519E-01	7.085E+06	9.392E+06	8.316E-01	2.439E+08	7.025E+19
1.5E+04.....	4.447E-01	7.906E+06	2.046E+07	8.375E-01	2.373E+08	4.815E+19
1.0E+04.....	1.263E-01	6.105E+07	9.242E+07	8.582E-01	2.180E+08	2.895E+19

TABLE 16
 $X(^4\text{He} = 0.3)$, $X(^{12}\text{C} = 0.7)$, $T_{\text{upstream}} = 3.0 \times 10^8$ K

Density (g cm^{-3})	Speed (cm s^{-1})	Thermal Width (cm)	Reaction Width (cm)	$\Delta\rho/\rho$	T_{crit} (K)	P_{isobaric} (ergs cm^{-3})
1.0E+08.....	1.442E+06	3.207E-03	2.826E-03	4.065E-01	4.265E+09	2.187E+25
8.0E+07.....	1.193E+06	4.572E-03	4.029E-01	4.304E-01	4.166E+09	1.612E+25
6.0E+07.....	9.099E+05	7.525E-03	6.692E-03	4.585E-01	4.007E+09	1.087E+25
4.0E+07.....	5.819E+05	1.581E-02	1.478E-01	4.967E-01	3.749E+09	6.212E+24
2.0E+07.....	2.109E+05	7.441E-02	7.617E-02	5.506E-01	3.214E+09	2.365E+24
1.5E+07.....	1.261E+05	1.588E-01	1.702E-01	5.688E-01	2.985E+09	1.578E+24
1.0E+07.....	6.215E+04	4.441E-01	4.995E-01	6.055E-01	2.705E+09	8.879E+23
8.0E+06.....	4.047E+04	8.379E-01	9.436E-01	6.191E-01	2.523E+09	6.459E+23
6.0E+06.....	2.721E+04	1.571E+00	1.878E+00	6.580E-01	2.370E+09	4.277E+23
4.0E+06.....	1.221E+04	5.058E+00	6.335E+00	6.606E-01	2.021E+09	2.385E+23
2.0E+06.....	3.399E+03	3.561E+01	3.744E+01	6.905E-01	1.521E+09	8.778E+22
1.5E+06.....	2.173E+03	7.611E+01	7.810E+01	7.008E-01	1.351E+09	5.814E+22
1.0E+06.....	1.248E+03	1.955E+02	2.088E+02	7.178E-01	1.172E+09	3.278E+22
8.0E+05.....	9.301E+02	3.117E+02	3.382E+02	7.266E-01	1.096E+09	2.404E+22
6.0E+05.....	6.437E+02	5.874E+02	6.297E+02	7.330E-01	1.011E+09	1.625E+22
4.0E+05.....	3.887E+02	1.427E+03	1.441E+03	7.422E-01	9.095E+08	9.524E+21
2.0E+05.....	1.664E+02	6.231E+03	6.095E+03	7.498E-01	7.673E+08	4.032E+21
1.5E+05.....	1.179E+02	1.145E+04	1.211E+04	7.422E-01	7.137E+08	2.878E+21
1.0E+05.....	7.357E+01	2.693E+04	3.185E+04	7.370E-01	6.472E+08	1.821E+21
8.0E+04.....	5.560E+01	4.645E+04	5.672E+04	7.353E-01	6.093E+08	1.427E+21
6.0E+04.....	3.927E+01	8.830E+04	1.128E+05	7.235E-01	5.653E+08	1.049E+21
4.0E+04.....	2.409E+01	2.309E+05	2.705E+05	7.107E-01	5.002E+08	6.886E+20
2.0E+04.....	1.134E+01	1.010E+06	1.134E+06	6.635E-01	3.762E+08	3.455E+20
1.5E+04.....	8.445E+00	1.881E+06	2.380E+06	6.352E-01	3.397E+08	2.625E+20
1.0E+04.....	5.558E+00	4.588E+06	6.718E+06	6.021E-01	3.223E+08	1.807E+20

TABLE 17
 $X(^4\text{He} = 0.3)$, $X(^{12}\text{C} = 0.7)$, $T_{\text{upstream}} = 2.0 \times 10^8 \text{ K}$

Density (g cm^{-3})	Speed (cm s^{-1})	Thermal Width (cm)	Reaction Width (cm)	$\Delta\rho/\rho$	T_{crit} (K)	P_{isobaric} (ergs cm^{-3})
1.0E+08	1.426E+06	3.231E-03	2.846E-03	4.078E-01	4.260E+09	2.174E+25
8.0E+07	1.179E+06	4.620E-03	4.082E-03	4.334E-01	4.162E+09	1.602E+25
6.0E+07	8.978E+05	7.580E-03	6.817E-03	4.608E-01	4.001E+09	1.079E+25
4.0E+07	5.775E+05	1.587E-02	1.469E-02	5.008E-01	3.746E+09	6.158E+24
2.0E+07	2.053E+05	7.550E-02	7.746E-02	5.550E-01	3.204E+09	2.336E+24
1.5E+07	1.260E+05	1.610E-01	1.710E-01	5.826E-01	3.012E+09	1.555E+24
1.0E+07	6.014E+04	4.559E-01	5.062E-01	6.159E-01	2.694E+09	8.720E+23
8.0E+06	3.882E+04	8.686E-01	9.769E-01	6.243E-01	2.507E+09	6.327E+23
6.0E+06	2.641E+04	1.606E+00	2.131E+00	6.586E-01	2.360E+09	4.172E+23
4.0E+06	1.193E+04	5.120E+00	6.395E+00	6.676E-01	2.014E+09	2.309E+23
2.0E+06	3.289E+03	3.577E+01	4.021E+01	7.039E-01	1.530E+09	8.322E+22
1.5E+06	2.030E+03	7.967E+01	8.606E+01	7.158E-01	1.337E+09	5.440E+22
1.0E+06	1.134E+03	2.048E+02	2.303E+02	7.370E-01	1.159E+09	2.994E+22
8.0E+05	8.029E+02	3.560E+02	3.686E+02	7.489E-01	1.070E+09	2.161E+22
6.0E+05	5.412E+02	6.786E+02	7.288E+02	7.591E-01	9.859E+08	1.426E+22
4.0E+05	3.112E+02	1.726E+03	1.824E+03	7.808E-01	8.818E+08	8.033E+21
2.0E+05	1.160E+02	8.642E+03	8.526E+03	7.960E-01	7.371E+08	3.159E+21
1.5E+05	7.755E+01	1.680E+04	1.837E+04	7.955E-01	6.845E+08	2.190E+21
1.0E+05	4.329E+01	4.492E+04	5.574E+04	7.991E-01	5.961E+08	1.334E+21
8.0E+04	3.139E+01	7.894E+04	1.003E+05	7.948E-01	5.577E+08	1.026E+21
6.0E+04	2.030E+01	1.627E+05	1.950E+05	7.900E-01	5.049E+08	7.382E+20
4.0E+04	1.163E+01	4.104E+05	4.250E+05	7.757E-01	4.336E+08	4.713E+20
2.0E+04	4.461E+00	2.047E+06	2.684E+06	7.487E-01	3.520E+08	2.263E+20
1.5E+04	2.957E+00	4.243E+06	5.980E+06	7.367E-01	3.268E+08	1.686E+20
1.0E+04	1.647E+00	1.236E+07	2.011E+07	7.217E-01	2.971E+08	1.123E+20

TABLE 18
 $X(^4\text{He} = 0.3)$, $X(^{12}\text{C} = 0.7)$, $T_{\text{upstream}} = 1.5 \times 10^8 \text{ K}$

Density (g cm^{-3})	Speed (cm s^{-1})	Thermal Width (cm)	Reaction Width (cm)	$\Delta\rho/\rho$	T_{crit} (K)	P_{isobaric} (ergs cm^{-3})
1.0E+08	2.822E+06	1.262E-01	9.923E-02	3.480E-01	1.500E+08	2.168E+25
8.0E+07	-4.589E+05	9.023E-03	8.712E-03	4.286E-01	3.465E+09	1.597E+25
6.0E+07	-8.947E+05	2.973E-02	2.997E-02	4.625E-01	5.348E+09	1.075E+25
4.0E+07	6.911E+05	1.883E-01	1.868E-01	5.267E-01	3.802E+09	6.132E+24
2.0E+07	6.588E+04	1.226E-01	1.248E-01	5.658E-01	1.500E+08	2.322E+24
1.5E+07	1.269E+05	1.565E-01	1.679E-01	5.847E-01	3.000E+09	1.545E+24
1.0E+07	5.878E+04	4.672E-01	5.145E-01	6.173E-01	2.687E+09	8.648E+23
8.0E+06	3.770E+04	9.000E-01	1.004E+00	6.337E-01	2.494E+09	6.267E+23
6.0E+06	2.618E+04	1.622E+00	2.119E+00	6.557E-01	2.361E+09	4.126E+23
4.0E+06	1.178E+04	5.134E+00	6.239E+00	6.834E-01	2.013E+09	2.276E+23
2.0E+06	3.103E+03	3.950E+01	4.431E+01	7.089E-01	1.501E+09	8.128E+22
1.5E+06	2.019E+03	7.866E+01	8.877E+01	7.278E-01	1.339E+09	5.283E+22
1.0E+06	1.044E+03	2.207E+02	2.423E+02	7.460E-01	1.138E+09	2.876E+22
8.0E+05	7.598E+02	3.741E+02	4.095E+02	7.581E-01	1.060E+09	2.060E+22
6.0E+05	5.048E+02	7.347E+02	7.713E+02	7.756E-01	9.735E+08	1.342E+22
4.0E+05	2.802E+02	1.924E+03	1.967E+03	7.911E-01	8.662E+08	7.396E+21
2.0E+05	9.727E+01	1.047E+04	1.105E+04	8.160E-01	7.034E+08	2.772E+21
1.5E+05	6.228E+01	2.073E+04	2.478E+04	8.198E-01	6.596E+08	1.880E+21
1.0E+05	3.256E+01	5.538E+04	7.689E+04	8.203E-01	5.747E+08	1.111E+21
8.0E+04	2.315E+01	1.034E+05	1.313E+05	8.243E-01	5.385E+08	8.413E+20
6.0E+04	1.422E+01	2.261E+05	2.390E+05	8.194E-01	4.690E+08	5.942E+20
4.0E+04	7.559E+00	5.992E+05	6.444E+05	8.143E-01	4.024E+08	3.710E+20
2.0E+04	2.581E+00	3.454E+06	4.887E+06	7.982E-01	3.297E+08	1.729E+20
1.5E+04	1.618E+00	7.830E+06	1.210E+07	7.900E-01	3.054E+08	1.275E+20
1.0E+04	8.328E-01	2.328E+07	1.424E+07	7.773E-01	2.794E+08	8.372E+19

TABLE 19
 $X(^4\text{He} = 0.3)$, $X(^{12}\text{C} = 0.7)$, $T_{\text{upstream}} = 1.0 \times 10^8$ K

Density (g cm^{-3})	Speed (cm s^{-1})	Thermal Width (cm)	Reaction Width (cm)	$\Delta\rho/\rho$	T_{crit} (K)	P_{isobaric} (ergs cm^{-3})
1.0E+08.....	1.412E+06	3.286E-03	2.848E-03	4.149E-01	4.258E+09	2.162E+25
8.0E+07.....	1.167E+06	4.667E-03	4.071E-03	4.375E-01	4.155E+09	1.592E+25
6.0E+07.....	8.866E+05	7.611E-03	6.814E-03	4.642E-01	3.997E+09	1.071E+25
4.0E+07.....	5.681E+05	1.598E-02	1.476E-02	5.036E-01	3.739E+09	6.108E+24
2.0E+07.....	2.008E+05	7.684E-02	7.882E-02	5.585E-01	3.196E+09	2.310E+24
1.5E+07.....	1.253E+05	1.580E-01	1.680E-01	5.921E-01	2.997E+09	1.535E+24
1.0E+07.....	5.828E+04	4.682E-01	5.233E-01	6.137E-01	2.684E+09	8.581E+23
8.0E+06.....	3.733E+04	8.986E-01	1.013E+00	6.297E-01	2.493E+09	6.212E+23
6.0E+06.....	2.589E+04	1.634E+00	2.136E+00	6.558E-01	2.356E+09	4.083E+23
4.0E+06.....	1.162E+04	5.260E+00	6.373E+00	6.866E-01	2.008E+09	2.246E+23
2.0E+06.....	3.262E+03	3.561E+01	4.176E+01	7.197E-01	1.529E+09	7.957E+22
1.5E+06.....	2.004E+03	7.652E+01	9.049E+01	7.356E-01	1.359E+09	5.147E+22
1.0E+06.....	1.080E+03	2.161E+02	2.452E+02	7.604E-01	1.152E+09	2.775E+22
8.0E+05.....	7.446E+02	3.772E+02	4.184E+02	7.676E-01	1.060E+09	1.973E+22
6.0E+05.....	4.874E+02	6.980E+02	8.244E+02	7.846E-01	9.815E+08	1.271E+22
4.0E+05.....	2.653E+02	1.960E+03	2.164E+03	8.012E-01	8.822E+08	6.859E+21
2.0E+05.....	8.211E+01	1.204E+04	1.327E+04	8.313E-01	7.023E+08	2.436E+21
1.5E+05.....	4.491E+01	2.713E+04	3.361E+04	8.414E-01	6.223E+08	1.606E+21
1.0E+05.....	2.546E+01	5.425E+04	8.939E+04	8.190E-01	5.578E+08	9.094E+20
8.0E+04.....	1.710E+01	1.100E+05	1.894E+05	8.348E-01	5.168E+08	6.722E+20
6.0E+04.....	1.072E+01	1.902E+05	3.275E+05	8.149E-01	4.773E+08	4.608E+20
4.0E+04.....	4.576E+00	7.527E+05	1.115E+06	8.355E-01	3.809E+08	2.769E+20
2.0E+04.....	1.335E+00	6.708E+06	1.083E+07	8.460E-01	3.038E+08	1.225E+20
1.5E+04.....	7.661E-01	1.574E+07	1.007E+07	8.423E-01	2.816E+08	8.886E+19
1.0E+04.....	3.654E-01	4.692E+07	3.275E+07	8.252E-01	2.573E+08	5.722E+19

TABLE 20
 $X(^4\text{He} = 0.3)$, $X(^{12}\text{C} = 0.7)$, $T_{\text{upstream}} = 8.0 \times 10^7$ K

Density (g cm^{-3})	Speed (cm s^{-1})	Thermal Width (cm)	Reaction Width (cm)	$\Delta\rho/\rho$	T_{crit} (K)	P_{isobaric} (ergs cm^{-3})
1.0E+08.....	1.407E+06	3.248E-03	2.812E-03	4.139E-01	4.258E+09	2.160E+25
8.0E+07.....	1.164E+06	4.648E-03	4.038E-03	4.380E-01	4.156E+09	1.590E+25
6.0E+07.....	8.846E+05	7.654E-03	6.825E-03	4.653E-01	3.996E+09	1.070E+25
4.0E+07.....	5.658E+05	1.615E-02	1.501E-02	5.079E-01	3.738E+09	6.098E+24
2.0E+07.....	2.000E+05	7.711E-02	7.908E-02	5.593E-01	3.195E+09	2.305E+24
1.5E+07.....	1.248E+05	1.587E-01	1.674E-01	5.912E-01	2.995E+09	1.531E+24
1.0E+07.....	5.793E+04	4.706E-01	5.230E-01	6.215E-01	2.682E+09	8.555E+23
8.0E+06.....	3.707E+04	9.058E-01	1.028E+00	6.324E-01	2.490E+09	6.191E+23
6.0E+06.....	2.668E+04	1.568E+00	1.969E+00	6.714E-01	2.373E+09	4.067E+23
4.0E+06.....	1.208E+04	5.012E+00	6.549E+00	6.964E-01	2.029E+09	2.235E+23
2.0E+06.....	3.481E+03	3.237E+01	4.393E+01	7.117E-01	1.554E+09	7.895E+22
1.5E+06.....	2.129E+03	6.879E+01	8.402E+01	7.350E-01	1.358E+09	5.098E+22
1.0E+06.....	1.118E+03	1.979E+02	2.577E+02	7.563E-01	1.179E+09	2.740E+22
8.0E+05.....	7.781E+02	3.436E+02	4.338E+02	7.756E-01	1.078E+09	1.943E+22
6.0E+05.....	4.963E+02	7.123E+02	8.350E+02	7.864E-01	9.768E+08	1.247E+22
4.0E+05.....	2.623E+02	2.063E+03	2.230E+03	8.136E-01	8.432E+08	6.676E+21
2.0E+05.....	8.297E+01	1.145E+04	1.405E+04	8.420E-01	6.822E+08	2.321E+21
1.5E+05.....	4.719E+01	2.792E+04	3.430E+04	8.486E-01	6.305E+08	1.511E+21
1.0E+05.....	2.008E+01	6.699E+04	9.840E+04	8.378E-01	5.302E+08	8.380E+20
8.0E+04.....	1.342E+01	1.359E+05	2.016E+05	8.501E-01	4.870E+08	6.116E+20
6.0E+04.....	8.024E+00	2.374E+05	3.668E+05	8.233E-01	4.282E+08	4.121E+20
4.0E+04.....	3.331E+00	5.646E+05	9.406E+05	7.846E-01	3.507E+08	2.418E+20
2.0E+04.....	1.009E+00	4.231E+06	5.621E+06	7.991E-01	2.978E+08	1.033E+20
1.5E+04.....	5.778E-01	1.164E+07	1.286E+07	8.202E-01	2.767E+08	7.407E+19
1.0E+04.....	2.687E-01	4.784E+07	4.544E+07	8.310E-01	2.574E+08	4.706E+19

TABLE 21
 $X(^4\text{He} = 0.3)$, $X(^{12}\text{C} = 0.7)$, $T_{\text{upstream}} = 6.0 \times 10^7$ K

Density (g cm^{-3})	Speed (cm s^{-1})	Thermal Width (cm)	Reaction Width (cm)	$\Delta\rho/\rho$	T_{crit} (K)	P_{isobaric} (ergs cm^{-3})
1.0E+08	1.407E+06	3.179E-03	2.815E-03	4.124E-01	4.253E+09	2.158E+25
8.0E+07	1.161E+06	4.572E-03	4.014E-03	4.361E-01	4.154E+09	1.588E+25
6.0E+07	8.827E+05	7.646E-03	6.814E-03	4.669E-01	3.995E+09	1.069E+25
4.0E+07	5.643E+05	1.615E-02	1.478E-02	5.093E-01	3.736E+09	6.088E+24
2.0E+07	1.992E+05	7.739E-02	7.949E-02	5.604E-01	3.194E+09	2.300E+24
1.5E+07	1.243E+05	1.591E-01	1.677E-01	5.918E-01	2.994E+09	1.527E+24
1.0E+07	5.763E+04	4.725E-01	5.220E-01	6.210E-01	2.681E+09	8.530E+23
8.0E+06	3.686E+04	9.085E-01	1.014E+00	6.366E-01	2.489E+09	6.171E+23
6.0E+06	2.667E+04	1.567E+00	1.902E+00	6.614E-01	2.379E+09	4.051E+23
4.0E+06	1.212E+04	5.000E+00	6.206E+00	6.849E-01	2.034E+09	2.224E+23
2.0E+06	3.551E+03	3.115E+01	4.023E+01	7.222E-01	1.567E+09	7.838E+22
1.5E+06	2.209E+03	5.862E+01	8.122E+01	7.169E-01	1.398E+09	5.053E+22
1.0E+06	1.170E+03	1.820E+02	2.445E+02	7.562E-01	1.178E+09	2.707E+22
8.0E+05	7.421E+02	3.485E+02	4.096E+02	7.730E-01	1.053E+09	1.916E+22
6.0E+05	5.326E+02	5.053E+02	8.796E+02	7.556E-01	1.000E+09	1.225E+22
4.0E+05	2.289E+02	1.592E+03	2.111E+03	7.922E-01	8.723E+08	6.514E+21
2.0E+05	8.253E+01	1.184E+04	1.555E+04	8.381E-01	6.721E+08	2.220E+21
1.5E+05	4.491E+01	2.845E+04	4.106E+04	8.531E-01	6.168E+08	1.428E+21
1.0E+05	1.011E+01	8.214E+04	1.164E+05	8.060E-01	4.366E+08	7.744E+20
8.0E+04	8.368E+00	2.253E+05	3.226E+05	8.478E-01	4.189E+08	5.570E+20
6.0E+04	5.496E+00	3.974E+05	6.338E+05	8.325E-01	3.680E+08	3.677E+20
4.0E+04	2.141E+00	1.279E+06	1.977E+06	8.462E-01	3.271E+08	2.091E+20
2.0E+04	6.224E-01	8.952E+06	9.155E+06	8.452E-01	2.793E+08	8.496E+19
1.5E+04	3.390E-01	2.367E+07	2.195E+07	8.587E-01	2.592E+08	5.982E+19
1.0E+04	1.821E-01	5.236E+07	7.635E+07	8.411E-01	2.464E+08	3.721E+19

tance, as indicated by the black arrows, is the critical temperature of 6.75×10^8 K. The type of analysis done for Figure 8 is repeated for all 525 different initial conditions considered in this survey.

The critical temperature of deflagrations propagating through a pure helium composition is shown in Figure 9,

through a half-helium and half-carbon composition in Figure 10, and through a composition of 30% helium and 70% carbon in Figure 11. The x -axis gives the upstream mass density, the y -axis the critical temperature, and each colored curve corresponds to a different upstream temperature. All three compositions have critical temperatures

TABLE 22
 $X(^4\text{He} = 0.3)$, $X(^{12}\text{C} = 0.7)$, $T_{\text{upstream}} = 4.0 \times 10^7$ K

Density (g cm^{-3})	Speed (cm s^{-1})	Thermal Width (cm)	Reaction Width (cm)	$\Delta\rho/\rho$	T_{crit} (K)	P_{isobaric} (ergs cm^{-3})
1.0E+08	1.404E+06	3.152E-03	2.783E-03	4.130E-01	4.254E+09	2.155E+25
8.0E+07	1.159E+06	4.543E-03	3.993E-03	4.371E-01	4.154E+09	1.587E+25
6.0E+07	8.810E+05	7.599E-03	6.755E-03	4.670E-01	3.994E+09	1.067E+25
4.0E+07	5.630E+05	1.610E-02	1.472E-02	5.097E-01	3.733E+09	6.079E+24
2.0E+07	1.983E+05	7.743E-02	8.011E-02	5.591E-01	3.192E+09	2.295E+24
1.5E+07	1.238E+05	1.598E-01	1.716E-01	5.893E-01	2.991E+09	1.524E+24
1.0E+07	5.749E+04	4.746E-01	5.271E-01	6.230E-01	2.679E+09	8.506E+23
8.0E+06	3.662E+04	9.115E-01	1.049E+00	6.351E-01	2.486E+09	6.151E+23
6.0E+06	2.657E+04	1.566E+00	2.226E+00	6.900E-01	2.377E+09	4.037E+23
4.0E+06	1.216E+04	4.980E+00	6.050E+00	6.799E-01	2.036E+09	2.214E+23
2.0E+06	3.498E+03	2.704E+01	3.998E+01	6.857E-01	1.570E+09	7.784E+22
1.5E+06	1.920E+03	4.751E+01	7.166E+01	6.574E-01	1.339E+09	5.011E+22
1.0E+06	1.040E+03	1.266E+02	1.781E+02	7.020E-01	1.153E+09	2.678E+22
8.0E+05	7.649E+02	2.233E+02	3.376E+02	7.181E-01	1.081E+09	1.892E+22
6.0E+05	4.087E+02	3.539E+02	5.346E+02	6.823E-01	9.394E+08	1.206E+22
4.0E+05	2.147E+02	1.519E+03	2.545E+03	7.929E-01	8.538E+08	6.372E+21
2.0E+05	7.342E+01	8.861E+03	1.271E+04	8.161E-01	6.694E+08	2.134E+21
1.5E+05	3.704E+01	1.899E+04	3.073E+04	8.102E-01	5.934E+08	1.357E+21
1.0E+05	7.303E+00	1.282E+05	1.926E+05	8.115E-01	3.962E+08	7.206E+20
8.0E+04	5.053E+00	2.606E+05	3.779E+05	8.204E-01	3.066E+08	3.295E+20
6.0E+04	1.656E+00	4.075E+05	4.308E+05	7.657E-01	3.658E+08	5.106E+20
4.0E+04	5.726E+00	3.340E+05	1.748E+06	7.988E-01	4.000E+07	1.804E+20

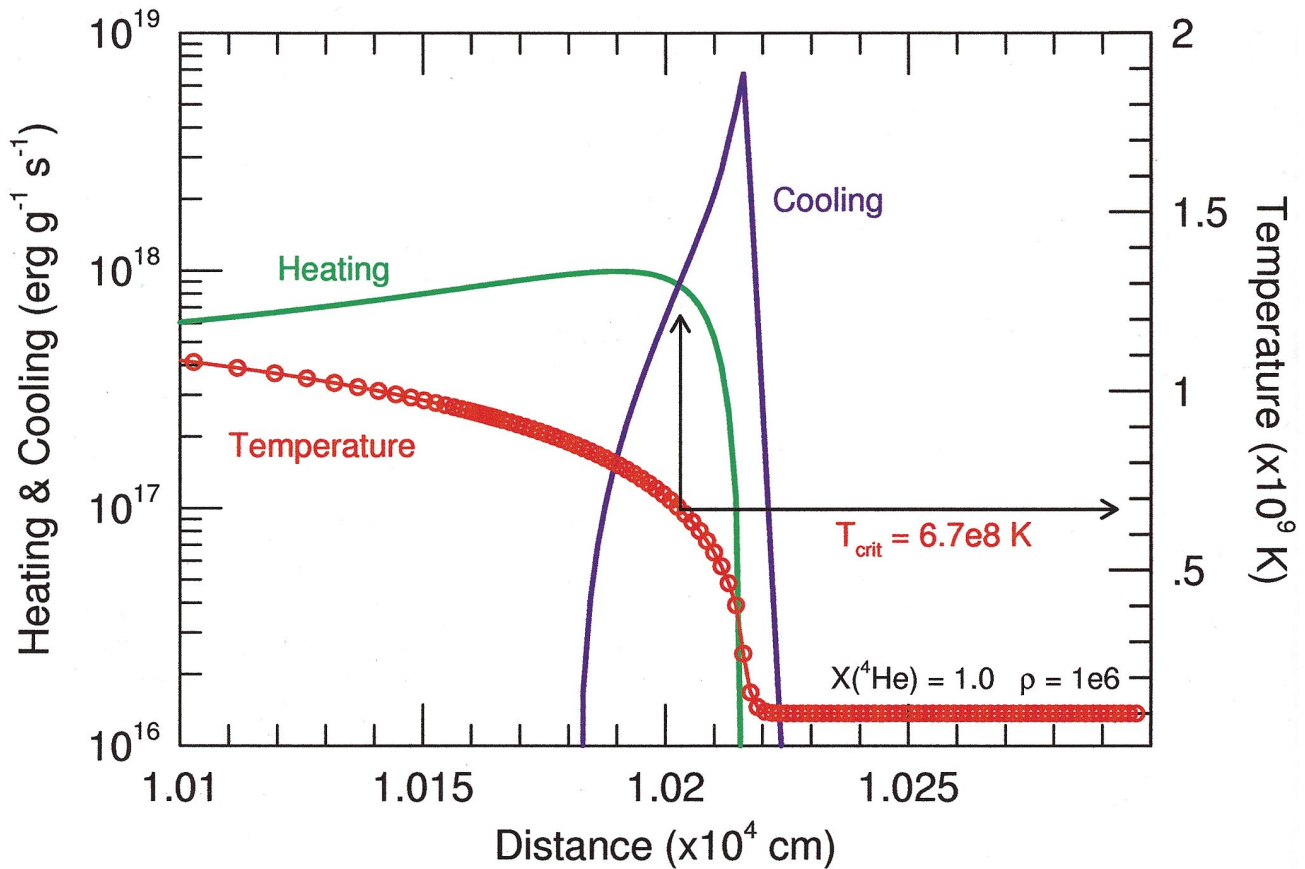


FIG. 8.—Obtaining the critical temperature of a deflagration. The x-axis gives the distance, the left y-axis gives the energy rates, and the right y-axis gives the temperature. A laminar deflagration is propagating into pure helium at an upstream density of 10^6 g cm^{-3} and an upstream temperature of 10^8 K . The red curve shows the deflagration's temperature profile, and the grid points used in the calculation are shown by the open circles. The purple curve shows the thermal energy transport rate, labeled “cooling,” and the green curve shows the nuclear energy generation rate, labeled “heating.” The black arrows indicate that the nuclear energy generation rate equals the thermal energy transport rate at a distance of $1.02 \times 10^4 \text{ cm}$, which corresponds to the deflagration's critical temperature of $6.75 \times 10^8 \text{ K}$.

that are largely independent of the upstream temperature and much more dependent on the upstream composition. This is because the properties of a deflagration are determined by the reaction kinetics and thermal transport within the flame front at the critical temperature. Consequently, the critical temperature depends more on the composition than on the upstream temperature.

The critical temperatures for pure helium compositions rise to a maximum at about $\sim 10^7 \text{ g cm}^{-3}$ and decline for larger densities. This behavior has two causes. The first is that in a pure helium composition the $^{12}\text{C}(\alpha, \gamma)^{16}\text{O}$ reaction cannot operate until some carbon is produced by the triple- α reaction. In fact, contributions to the energy generation rate from the $^{12}\text{C}(\alpha, \gamma)^{16}\text{O}$ reaction never dominate the energetics within the flame's reaction width for pure helium compositions. Pure helium deflagrations are denied the large energy release from the $^{12}\text{C}(\alpha, \gamma)^{16}\text{O}$ reaction, which dominate the energy release at high densities in compositions with a significant initial carbon abundance (also see the discussion of Fig. 6). The second reason is that as the density becomes larger the effects from degeneracy and relativity are increased (see Fig. 2). Both relativity (which increases the average speed \bar{v} of the electrons) and degeneracy (which increases the mean free path λ of the electrons) increase the thermal conductivity $\sigma \propto \lambda \bar{v}$. Thus, the relatively suppressed heating rate from energy produced by nuclear reactions [$^{12}\text{C}(\alpha, \gamma)$ not operating] and the

increased cooling from a larger thermal conductivity (relativity and degeneracy) both act to decrease the critical temperature of pure helium deflagrations at large densities. In essence, cooling increases faster than heating at these densities ($1/\kappa$ versus \dot{S}/ρ in eq. [6]).

The critical temperatures for compositions with a significant initial carbon abundance do not show a pronounced maximum, and instead increase monotonically. This is because these compositions permit an energy release $^{12}\text{C}(\alpha, \gamma)^{16}\text{O}$ within their reaction widths, while the pure helium composition does not. Even though the thermal conductivity is still increasing because of the degenerate and relativistic electrons, the energy deposited from the $^{12}\text{C}(\alpha, \gamma)^{16}\text{O}$ is large enough and increases fast enough to compensate. Heating increases faster than cooling at the larger densities of compositions with a nonzero initial carbon abundance.

3.2. Thermal and Reactive Widths

The thermal width of the steady state helium deflagration is defined as the distance between where the temperature has reached 90% of its maximum and where the temperature has risen 10% above the upstream temperature (see Fig. 8). The reactive width is defined as the distance between where the energy generation rate has reached 90% of its maximum value and where the temperature has risen 10% above the upstream temperature. These two widths are

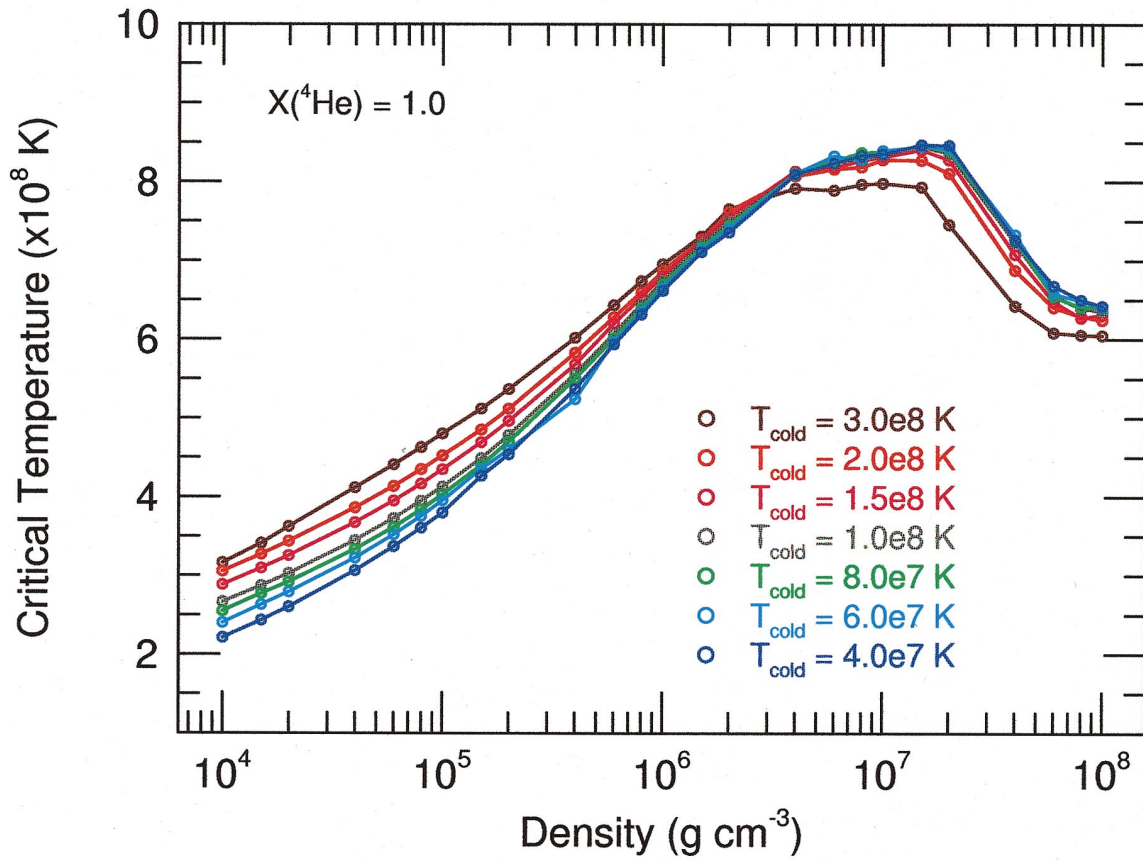


FIG. 9.—Critical temperature of laminar deflagrations propagating into pure helium. The upstream density is given on the x-axis, and the critical temperature is given on the y-axis. Each labeled colored curve corresponds to a different upstream temperature.

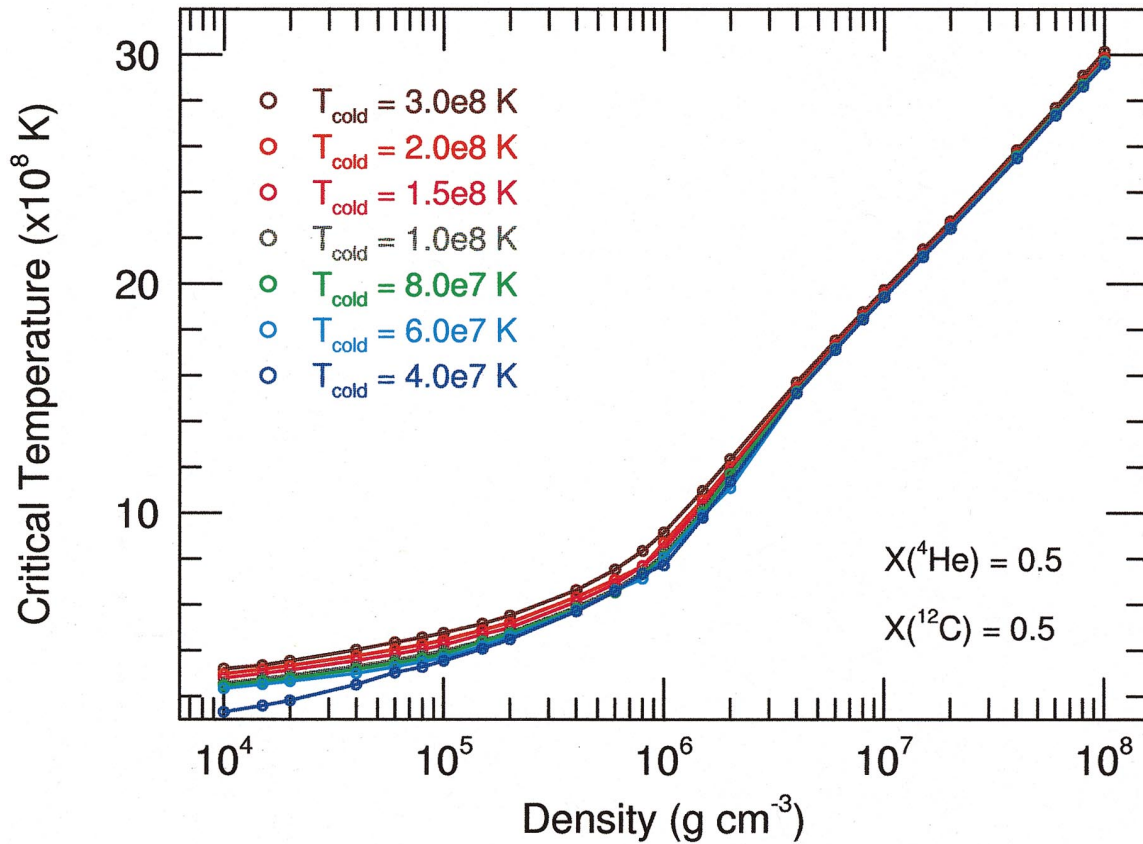


FIG. 10.—Critical temperatures of laminar deflagrations propagating into a half-helium $X(^4\text{He}) = 0.5$ and half-carbon $X(^{12}\text{C}) = 0.5$ mixture. The format is the same as in Figure 10.

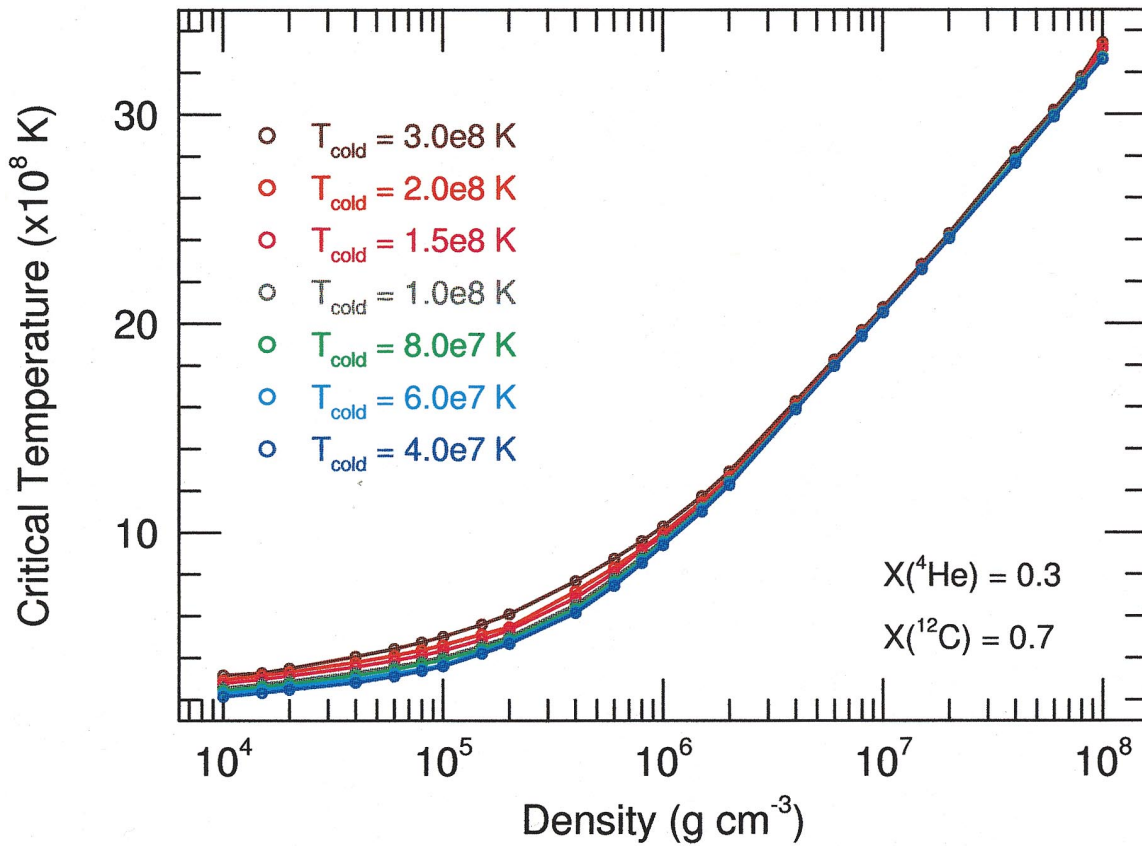


FIG. 11.—Critical temperatures of laminar deflagrations propagating into a $X(^4\text{He}) = 0.3$ and $X(^{12}\text{C}) = 0.7$ mixture. The format is the same as in Figure 10.

shown in Figure 12 as a function of the laminar flame speed for a half-helium and half-carbon composition at an upstream temperature of 10^8 K. The red curve corresponds to the thermal widths, and the purple curve represents the reactive widths. Both curves illustrate that the faster a laminar deflagration propagates, the thinner the flame front becomes. The widths listed in Tables 2–4 are useful for determining whether a steady state helium deflagration can propagate in a thin layer of fuel. If the width of the laminar flame is much larger than the dimensions of the fuel layer, then a steady state, laminar deflagration cannot propagate.

3.3. How Small a Matchhead Is Needed to Form a Deflagration?

Interesting questions about the types of initial conditions that can eventually generate a steady state helium deflagration can be addressed to zeroth order by using the order-of-magnitude estimates. An estimate of the minimum amount of mass, the trigger mass, necessary to sustain a steady state deflagration may be formed from equation (6):

$$M_{\text{trig}} \sim \frac{4}{3} \pi W_T^3 \rho \sim \frac{4}{3} \pi \rho \left(\frac{\lambda c E}{\dot{S}} \right)^{3/2}, \quad (10)$$

which is strongly dependent on the temperature through the nuclear energy generation rate \dot{S} and the specific thermal energy E . A corresponding trigger energy may be defined through

$$E_{\text{trig}} = (T - T_{\text{upstream}}) \frac{\partial E}{\partial T} M_{\text{trig}}. \quad (11)$$

The trigger energy curves represent the total thermal energy that must be deposited in order to propagate a steady state helium deflagration.

The minimum trigger quantities are shown in Figure 13 for a pure helium composition. The x-axis gives the temperature, the left-hand y-axis gives the minimum trigger mass, and the right-hand y-axis gives the minimum trigger energy. The critical temperature T_{crit} of laminar deflagrations is represented schematically by the vertical purple line and is labeled on the temperature axis. Each red trigger curve is labeled by the corresponding upstream density. The trigger curves define two distinct regions. Regions below any trigger-mass curve correspond to cases where the energy deposited in a given mass is unable to raise the temperature to the critical temperature T_{crit} . Disturbances in this region simply diffuse away, since the diffusion timescale is shorter than the burning timescale. Regions above any trigger-mass curve correspond to overdriven cases, where the burning timescale is smaller than the diffusion timescale. In this region the energy input is more than enough to raise the temperature to the critical temperature, and thus propagate a steady state wave.

The trigger curves and the critical temperature indicate three possible time evolutions of any given mass element. Several initial starting temperatures are shown in Figure 13 as the filled purple circles. The subsequent evolution of each mass is shown schematically by the purple arrows. The two purple circles below the trigger-mass curves simply diffuse away their perturbing energy, even if the perturbing energy is great enough to initially raise the temperature above the critical temperature. These masses are just too small to

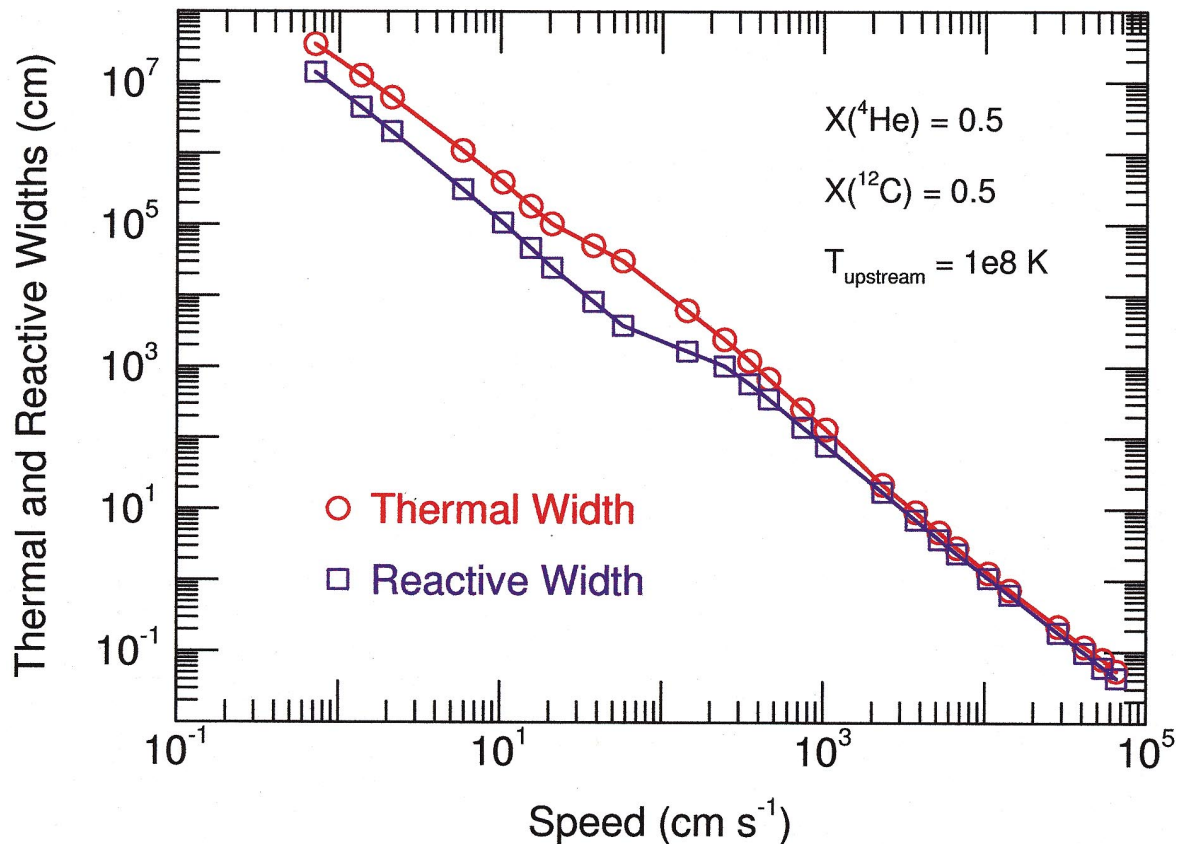


FIG. 12.—Thermal and reactive widths versus the steady state deflagration speed for a 50% helium–50% carbon composition and an upstream temperature of 10^8 K . The red curve corresponds to the thermal widths, and the purple curve represents the reactive widths. The faster a deflagration propagates, the thinner deflagration it becomes. If the width of a laminar flame is much larger than one of the dimensions in a layer of fuel, then a steady state deflagration cannot propagate in that direction.

sustain a steady state helium deflagration. The purple circle above the trigger-mass curves, but with a temperature below the critical temperature, is an underdriven disturbance. In this case, the disturbance is capable of raising its temperature through energy generated by nuclear burning to the requisite critical temperature. How long in time it takes to reach the steady state depends on the nuclear burning timescale at the initial temperature. The purple circle above the trigger-mass curves, and with a temperature above the critical temperature, is an overdriven disturbance. In this case, the disturbance initially propagates faster than the steady state value. The disturbance cools, and thus slows, as the excess energy is diffused away into the ambient medium. How long it takes for the overdriven disturbance to reach the steady state depends on how much greater the initial temperature is from the critical temperature.

This analysis of the types of initial conditions that can generate a steady state helium deflagration are based on the order-of-magnitude relations. The trigger mass may also be determined from solving the reaction-diffusion equations with various initial perturbations. The trigger masses derived from the order of magnitude appears to be no worse than about a factor of 3 different from what solutions from the reaction-diffusion equations yield, although a complete survey with the reaction-diffusion equations was not conducted.

3.4. With and without a Magnetic Field

There are times when a helium deflagration may be

subject to the effects of a strong magnetic field. Neutron stars with a strong magnetic field, for example, may confine their accreted pool of helium fuel to their polar regions. When a strong magnetic field is present, the largest changes to the properties of laminar deflagrations are probably due to changes in the thermal transport coefficients. The transport physics, approximations and subroutines of Potekhin & Yakovlev (1996, 1999) and A. Y. Potekhin (1999, private communication) are used below to assess quantitatively the changes to the laminar flame speed.

The thermal conductivity parallel to the direction of the magnetic field is shown in Figure 14. The x-axis gives the upstream mass density, and the y-axis gives the longitudinal thermal-transport coefficient. Curves for a magnetic field of 10^{12} G is shown as a solid red line, while a field strength of 0 G is shown as a dashed green line. Every oscillation of the red curves represents the population of a new Landau level. At a temperature of 10^6 K and densities less than $\sim 10^6 \text{ g cm}^{-3}$ the material is in the solid phase (see the melting line in Fig. 2), where electron-phonon scattering dominates contributions to the thermal conductivity. At larger densities the material is in the liquid phase, where ion-electron scattering dominates. These two conductivities match each other quite well in the transition region, so there is no discontinuity as the material undergoes the liquid-solid phase transition. At a temperature of 10^7 K , the Landau levels are thermally broadened, which reduces the amplitude of each oscillation. At a temperature of 10^8 K , the Landau levels are thermally broadened to the extent that the longitudinal conductivity becomes a monotonic function of the density

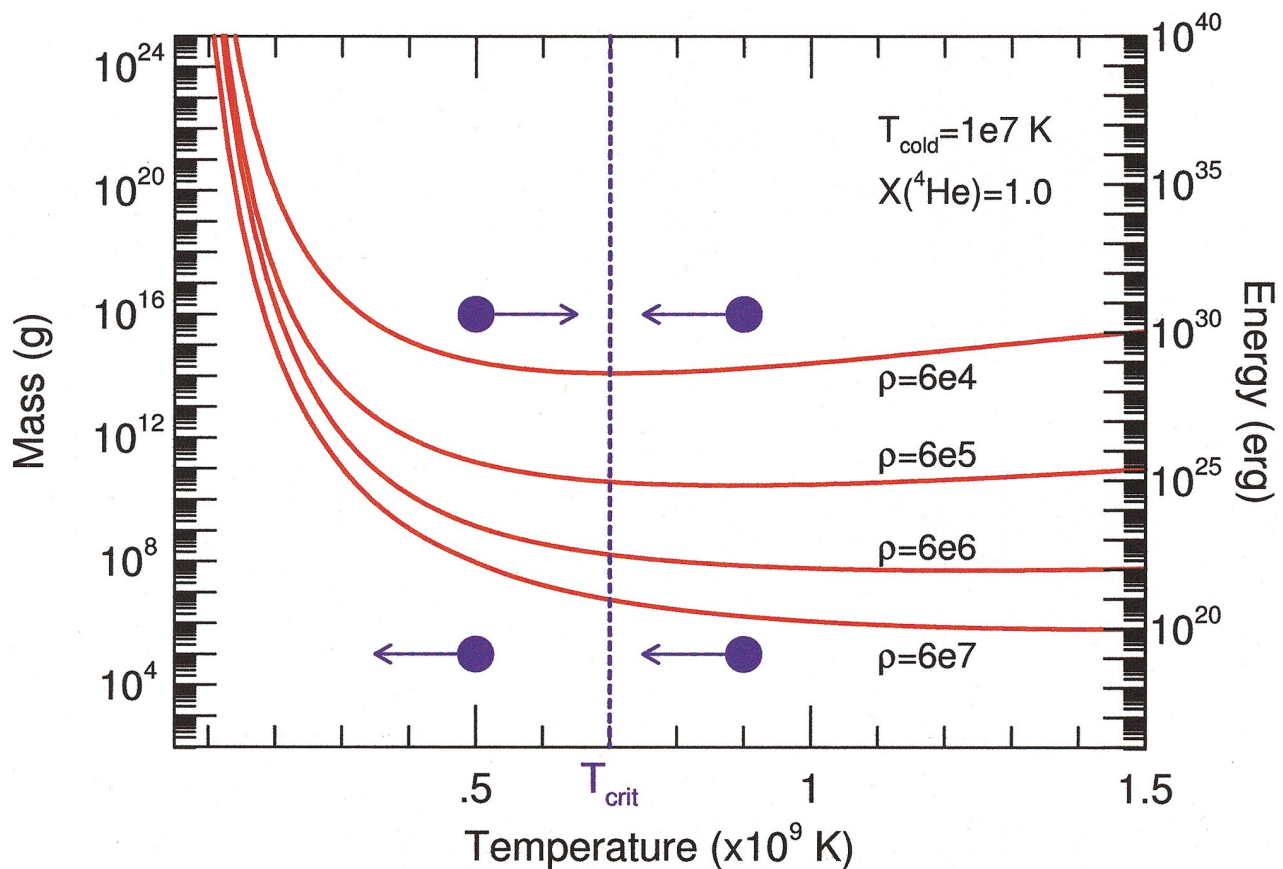


FIG. 13.—Trigger mass as a function of the perturbing temperature and density for pure helium compositions. The critical temperature T_{crit} , where heating from energy liberated by nuclear reactions is equal to cooling from thermal energy transport, is marked by the dashed line. Initial conditions below the trigger-mass curves, indicated by the crossed circles, cannot sustain a steady state wave and simply cool off on diffusive timescales. The general direction of the evolution is indicated by the arrows. Conditions initially above the curves can propagate deflagration waves, with the schematic evolution of several mass points indicated. The trigger energy, related to the trigger mass by eq. (10), is shown on the right-hand axis.

(Potekhin & Yakovlev 1996). The quantizing effects of the magnetic field also weaken as the density increases, with the longitudinal conductivity approaching the conductivity without a magnetic field (red curves coinciding with the green curves at high densities). Presence of any magnetic field reduces the maximum scattering-impact parameter, especially at low densities. This reduction decreases the Coulomb logarithm, and makes the longitudinal conductivity greater than the zero magnetic field conductivity (red curves on top of the green curves at low densities).

Figure 14 suggests that the difference between the longitudinal transport coefficient and the zero field transport coefficient becomes quite small as the temperature is increased. Since the critical temperatures of helium deflagrations are always greater than 2×10^8 K (the ignition temperature of helium), helium deflagrations that propagate parallel to the magnetic field lines do so at a speed that is not significantly different from the zero magnetic field flame speeds given in Tables 2–4. What small differences do exist can be accounted for by using the scaling relation of equation (6), namely, $V_{\text{cond}} \propto \sigma^{1/2}$.

The thermal conductivity perpendicular to the direction of the magnetic field is shown in Figure 15. The x -axis gives the upstream mass density, and the y -axis gives the transverse thermal-transport coefficient. Curves for a magnetic field of 10^{12} G are shown as solid red. Curves for a magnetic field of 0 G are the same as the green curves in Figure 14, and are off the scale of the y -axis in Figure 15. Thus, the

ratio of the transverse thermal-transport coefficient to the zero field thermal-transport coefficient is very large, about 5 orders of magnitude. If the scaling relation of equation (6) applies over such large changes, then helium deflagrations propagating in a direction perpendicular to the direction of the magnetic field travel at speeds that are a factor of $10^{5/2} \sim 300$ slower than the speeds listed in Tables 2–4. Figures 14 and 15 indicate that laminar helium deflagrations propagate ~ 300 times faster in directions parallel to the magnetic field than they propagate in directions perpendicular to the field lines. Any laminar helium deflagration that is initially symmetric rapidly becomes quite asymmetric.

4. SUMMARY

The physical properties of helium deflagrations have been assessed, with values for the speed, thermal width, reactive width, and density contrast given in Tables 2–4. While interpolation in the tables is the preferred method for incorporating the results into a subgrid model or a flame-tracking algorithm for hydrodynamic programs, fitting formulae of modest accuracy for the flame speed were presented in equation (9).

The physical properties were shown to be robust with respect to variation in the thermal-transport coefficients, the equation of state, and the nuclear reaction rates (owing to the large number of reaction channels available). However, flame speeds computed with very small networks

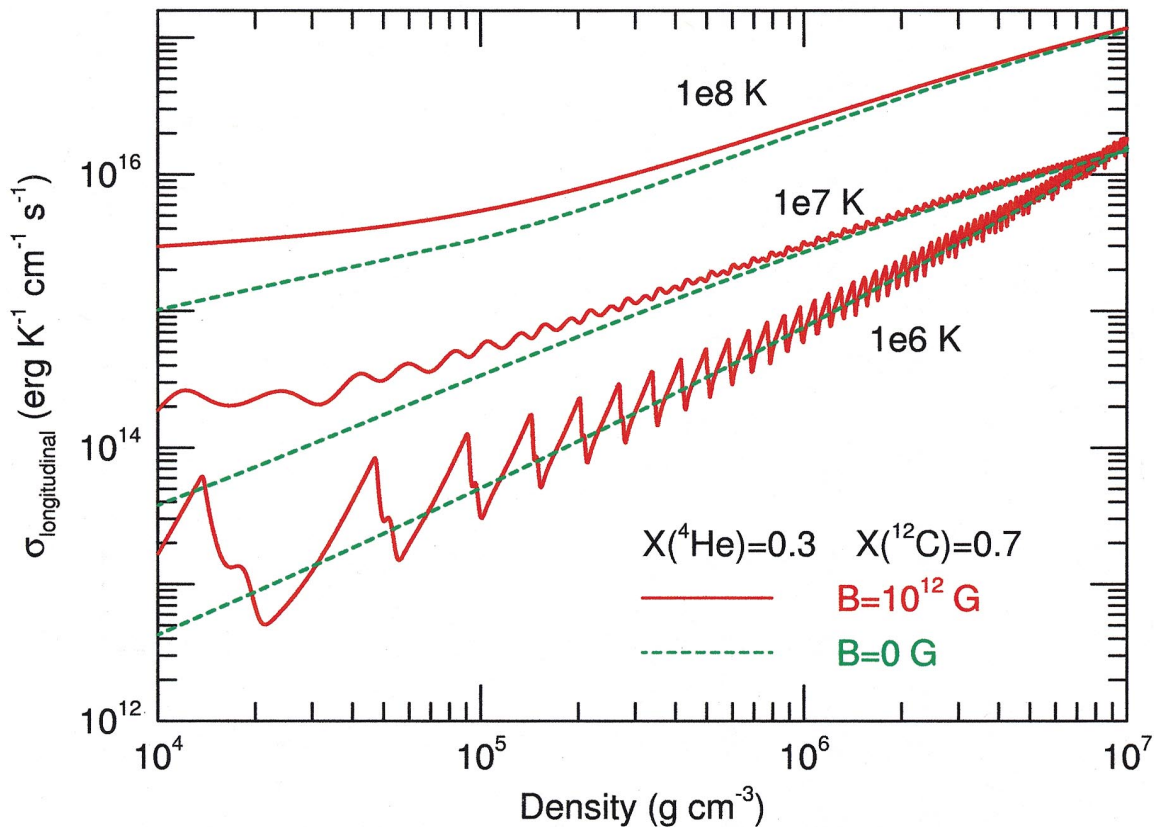


FIG. 14.—Longitudinal thermal conductivity as a function of density. The red curves at temperatures of 10^6 , 10^7 , and 10^8 K correspond to a magnetic field strength of 10^{12} G. The dashed green curves at the same temperatures correspond to zero magnetic field. The difference between the longitudinal transport coefficient and the zero field transport coefficient becomes smaller as the temperature is increased. Since the critical temperatures of helium deflagrations are always greater than 2×10^8 K, helium deflagrations along the magnetic field lines propagate at a speed that is not significantly different from the zero magnetic field flame speeds.

(2–3 isotopes) were shown to underestimate the flame speed by about 50%, while calculations that ignore the $P dV$ work terms in the energy equation were shown to yield flame speeds that overestimate the flame speed by about 40%. With the flame speeds almost independent of variations in the nuclear reaction rates, and the thermal conductivity being theoretically uncertain to about 30%, the physical properties of helium deflagrations given in Tables 2–22 should be correct to about 15%.

Caution is strongly advised in applying these results of helium and helium-metal flame properties to thin-shell helium flashes and X-ray bursts, since the calculated properties do not include the presence of any hydrogen. Subsonic and laminar hydrogen-burning fronts may play a major role in stellar models of an X-ray burst or a thin-shell helium flash. The present paper only surveys laminar deflagrations through helium and helium-metal compositions. A detailed survey of laminar deflagrations through pure hydrogen, hydrogen-helium, and hydrogen-helium-metal compositions is, at this writing, being investigated.

The calculated laminar helium deflagration speeds given in the tables are strict lower bounds. They are the slowest speeds at which a deflagration can propagate. Turbulent, bulk fluid motion, convection, and various hydrodynamic instabilities increase the laminar flame speed by either increasing the rate at which fuel crosses the flame front (e.g., a wrinkled flame front) or by mixing burned and unburned material. In fact, any planar deflagration treated in the density discontinuity approximation is unstable to infinitesimal

perturbations and becomes wrinkled (Landau & Lifshitz 1959). The linear stability analysis can be extended to incorporate a finite flame thickness and show that heat conduction stabilizes the smallest, fastest growing perturbations (Frankel & Sivashinsky 1982). Perturbations larger than the thermal width of the deflagration still wrinkle the flame front, but on longer timescales. Deflagrations which propagate in the radial direction of a star (opposite the direction of the gravitational force) are subject to Rayleigh-Taylor instabilities, since the density decreases behind the deflagration.

Hence, a strictly laminar flame is almost a complete fantasy under most astrophysical conditions because turbulence or convection generally prevails at the conditions where deflagrations occur. However, almost all of these formulae for the speed of a subsonic burning front propagating through turbulent or convectively unstable material have, for good physical reasons, the laminar flame speed in their expressions. Only in the limit in which the Froude number ($Fr = v^2/Lg$) is very small is the burning front likely to propagate at a speed which is independent of the laminar burning front speed (Khokhlov 1995; Niemeyer & Hillbrandt, 1995a, 1995b; Timmes & Niemeyer 1999). These parameterized expressions essentially attempt to describe how bulk fluid motions or various hydrodynamic instabilities increase the speed of burning front over and above the laminar flame speed. It is thus of some interest to those who apply such parameterized turbulent burning expressions in their stellar models to have reasonably precise

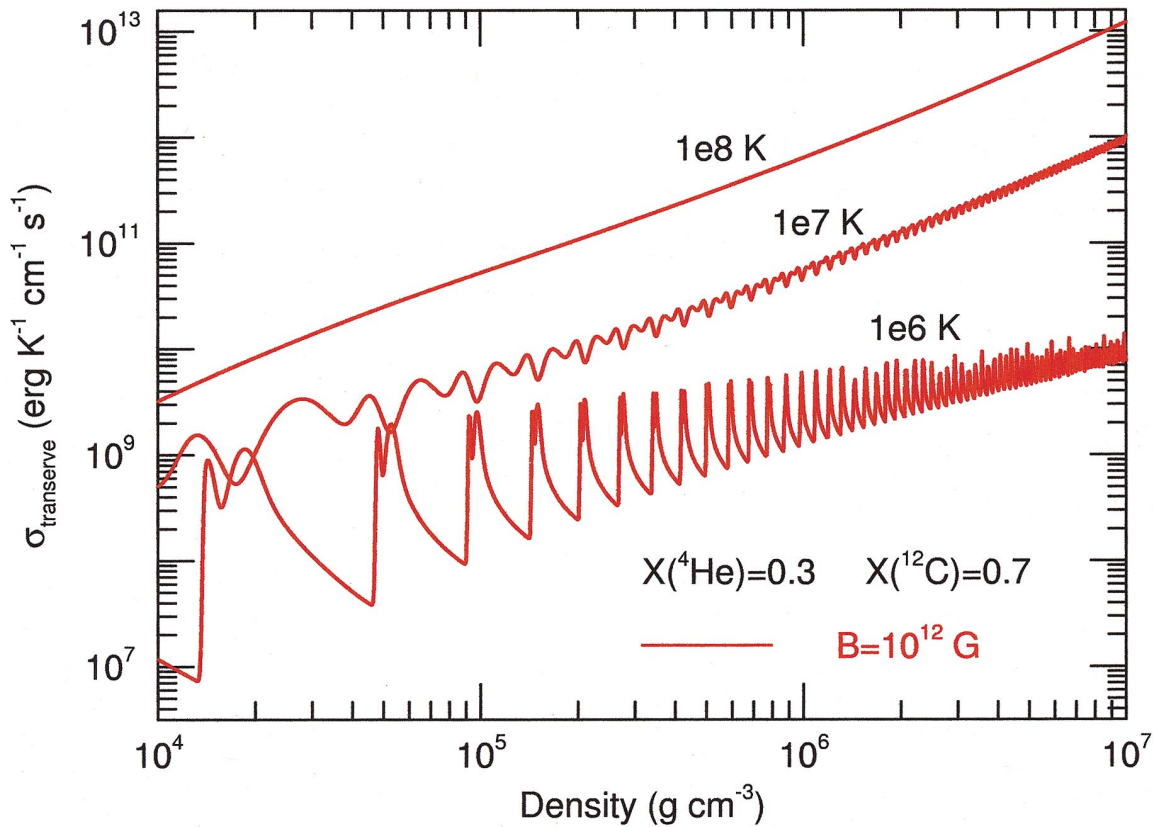


FIG. 15.—Transverse thermal conductivity as a function of density. The red curves at temperatures of 10^6 , 10^7 , and 10^8 K correspond to a magnetic field strength of 10^{12} G. Curves for a magnetic field of 0 G are the same as the green curves in Figure 14, and are off the scale of the y-axis in this figure. Thus, the ratio of the transverse transport coefficient to the zero field transport coefficient is about 5 orders of magnitude, which suppresses the propagation speeds of helium deflagrations perpendicular to the magnetic field by a factor of ~ 300 .

values for the laminar flame speed. While an idealized laminar flame front probably does not apply to most stellar situations, the lower bound laminar flame speed forms a vital ingredient in constructing better models of these stellar events.

The author thanks Lars Bildsten for providing his helium flame speeds in machine-readable form, Rob Hoffman for keeping the author's nuclear reaction database current, and

the members and affiliates of the Center on Astrophysical Thermonuclear Flashes for incinerating discussions. This work was supported by the Department of Energy under grant B341495 to the Center on Astrophysical Thermonuclear Flashes at the University of Chicago, the National Science Foundation under grant PHY94-07194 to the Institute for Theoretical Physics at the University of California at Santa Barbara, and a *Compton Gamma Ray Observatory* Postdoctoral Fellowship.

APPENDIX A

THERMAL TRANSPORT PROPERTIES

Below is shown the FORTRAN subroutine discussed in § 2.2 to calculate the thermal transport coefficients. Some execution efficiency has been sacrificed in order to gain clarity or shorten the printed length. An example is that multiple square roots of the same quantity are used instead of declaring a new variable and calculating the square root only once. It is also a straightforward exercise, left to the reader, to modify the routine to have it return analytic derivatives of the transport coefficients with respect to the temperature and density.

```

subroutine sig99(temp,den,xmass,zion,aion,ionmax,pep,xne,eta,opac)
implicit none
save
c..
c..this routine approximates the thermal transport coefficients.
c..
c..input:
c..temp=temperature temp (in K)
c..den=density den (in g/cm**3)
c..ionmax=number of isotopes in the composition

```



```

c..xmass=mass fractions of the composition
c..zion=number of protons in each isotope (charge of each isotope)
c..aion=number of protons + neutrons in each isotope (atomic weight)
c..pep=electron-positron pressure (in erg/cm**3)
c..xne=electron-positron number density (in 1/cm**3)
c..eta=electron degeneracy parameter (chemical potential / k T)
c..
c..output:
c..opac=the total opacity (in cm**2/g)
c..
c..declare the pass
      integer ionmax
      double precision temp,den,xmass (ionmax),zion (ionmax),aion (ionmax),
1      pep,xne,eta,opac

c..declare the internal variables
      integer iz,i
      double precision xmu,t6,orad,ocond,ytot1,ymass,abar,zbar,w(6),xh,
1 xhe,xz,xkc,xkap,xkb,xka,dbar,oiben1,d0log,xka1,xkw,xkaz,dbar1log,
2 dbar2log,oiben2,t4,t4r,t44,t45,t46,ck1,ck3,ck2,ck4,ck5,ck6,xkcx,
3 xkcy,xkcz,ochrs,th,fact,facetax,faceta,ocompt,tcut,cutfac,xkf,
4 dlog10,zdel,zdell10,eta0,eta02,thpl,thpla,cfac1,cfac2,oh,pefac,
5 pefacl,pefac1,dnefac,wpar2,walf,walf10,thx,thy,thc,farg,ffac,
6 xmas,ymas,wfac,cint,vie,cie,tpe,yg,xrel,beta2,jy,vee,cee,ov1,ov,
7 drel,drell10,drelim

c..various physical and derived constants
c..con2=con1*sqrt(4*pi*e*e/me) meff=hbar/(me*c)*(3*pi**2)**(1/3)
c..weid=(pi*kerg)**2/(3*me) iec=4*e**4*me/(3*pi*hbar**3)
c..xec=hbar/kerg*e*sqrt(4*pi/me)
      double precision third,twoth,pi,avo,c,ssol,asol,zbound,t7peek,
1 con2,k2c,meff,weid,iec,xec,rt3
      parameter (third=1.0d0/3.0d0,twoth=2.0d0*third,
1 pi=3.1415926535897932384d0,avo=6.0221367d23,
2 c=2.99792458d10,ssol=5.67050407222d-5,asol=4.0d0*ssol/c,
3 zbound=0.1d0,t7peek=1.0d20,k2c=4.0d0/3.0d0*asol*c,
4 meff=1.194648642401440d-10,weid=6.884326138694269d-5,
5 iec=1.754582332329132d16,xec=4.309054377592449d-7,
6 rt3=1.7320508075688772d0,con2=1.07726359439811217d-7)

c..initialize
      opac=0.0d0
      orad=0.0d0
      ocond=0.0d0
      oiben1=0.0d0
      oiben2=0.0d0
      ochrs=0.0d0
      oh=0.0d0
      ov=0.0d0
      zbar=0.0d0
      ytot1=0.0d0

c..set the composition variables
      do i=1,6
        w(i)=0.0d0
      enddo
      do i=1,ionmax
        iz=min(3,max(1,int(zion(i))))
        ymass=xmass(i)/aion(i)
        w(iz)=w(iz)+xmass(i)
        w(iz+3)=w(iz+3)+zion(i)*zion(i)*ymass
        zbar=zbar+zion(i)*ymass
        ytot1=ytot1+ymass
      enddo

```

```

abar=1.0d0/ytot1
zbar=zbar*abar
t6=temp*1.0d-6
xh=w(1)
xhe=w(2)
xz=w(3)

```

```

c..radiative section:

```

```

c..from iben apj 196 525 1975

```

```

  if (xh.lt.1.0e-5) then
    xmu=max(1.0d-99, w(4)+w(5)+w(6)-1.0d0)
    xkc=(2.019e-4*den/t6**1.7d0)**(2.425d0)
    xkap=1.0d0+xkc*(1.0d0+xkc/24.55d0)
    xkb=3.86d0+0.252d0*sqrt(xmu)+0.018d0*xmu
    xka=3.437d0*(1.25d0+0.488d0*sqrt(xmu)+0.092d0*xmu)
    dbar=exp(-xka+xkb*log(t6))
    oiben1=xkap*(den/dbar)**(0.67d0)
  endif

  if (.not.((xh.ge.1.0e-5).and.(t6.lt.1.0)).and.
1    .not.((xh.lt.1.0e-5).and.(xz.gt.zbound))) then
    if (t6.gt.1.0) then
      d0log=-(3.868d0+0.806d0*xh)+1.8d0*log(t6)
    else
      d0log=-(3.868d0+0.806d0*xh)+(3.42d0-0.52d0*xh)*log(t6)
    endif
    xka1=2.809d0*exp(-(1.74d0-0.755d0*xh)
1      *(log10(t6)-0.22d0+0.1375d0*xh)**2)
    xkw= 4.05d0*exp(-(0.306d0-0.04125d0*xh)
1      *(log10(t6)-0.18d0+0.1625d0*xh)**2)
    xkaz=50.0d0*xz*xka1*exp(-0.5206d0*((log(den)-d0log)/xkw)**2)
    dbar2log=-(4.283d0+0.7196d0*xh)+3.86d0*log(t6)
    dbar1log=-5.296d0+4.833d0*log(t6)
    if (dbar2log.lt.dbar1log) dbar1log=dbar2log
    oiben2=(den/exp(dbar1log))**(0.67d0)*exp(xkaz)
  endif

```

```

c..from christy apj 144 108 1966

```

```

  if ((t6.lt.1.5).and.(xh.ge.1.0e-5)) then
    t4=temp*1.0d-4
    t4r=sqrt(t4)
    t44=t4**4
    t45=t44*t4
    t46=t45*t4
    ck1=2.0d6/t44+2.1d0*t46
    ck3=4.0d-3/t44+2.0d-4/den**(0.25d0)
    ck2=4.5d0*t46+1.0d0/(t4*ck3)
    ck4=1.4d3*t4+t46
    ck5=1.0d6+0.1d0*t46
    ck6=20.0d0*t4+5.0d0*t44+t45
    xkcx=xh*(t4r/ck1+1.0d0/ck2)
    xkcy=xhe*(1.0d0/ck4+1.5d0/ck5)
    xkcz=xz*(t4r/ck6)
    ochrs=pep*(xkcx+xkcy+xkcz)
  endif

```

```

c..opacity in presence of hydrogen

```

```

  if (xh.ge.1.0e-5) then
    if (t6.lt.1.0) then
      orad=ochrs
    else if (t6.le.1.5) then
      orad=2.0d0*(ochrs*(1.5d0-t6)+oiben2*(t6-1.0d0))
    else
      orad=oiben2
    endif
  endif

```

```

c..opacity in absence of hydrogen
  else
    if (xz .gt. zbound) then
      orad=oiben1
    else
      orad=oiben1*(xz/zbound) + oiben2*((zbound-xz)/zbound)
    end if
  end if

c..add in the compton scattering opacity, weaver et al. apj 1978 225 1021
  th=min(511.0d0,temp*8.617d-8)
  fact=1.0d0+2.75d-2*th-4.88d-5*th*th
  facetax=1.0d100
  if (eta .le. 500.0) facetax=exp(0.522d0*eta-1.563d0)
  faceta=1.0d0+facetax
  ocompt=6.65205d-25/(fact*faceta)*xne/den
  orad=orad+ocompt

c..cutoff radiative opacity when  $4kt/hbar$  is less than the plasma frequency
  tcut=con2*sqrt(xne)
  if (temp.lt.tcut) then
    if (tcut.gt.200.0*temp) then
      orad=orad*2.658d86
    else
      cutfac=exp(tcut/temp-1.0d0)
      orad=orad*cutfac
    end if
  end if

c..fudge molecular opacity for low temps
  xkf=t7peek*den*(temp*1.0d-7)**4
  orad=xkf*orad/(xkf+orad)

c..conductivity section:
c..drel is the dividing line between nondegenerate and degenerate regions,
c..taken from clayton eq. 2-34. if the density is larger than drel, then
c..use the degenerate expressions. if the density is smaller than
c..drelim, use the non-degenerate formulas. in between drel and drelim,
c..apply a smooth blending of the two.
  drel=2.4d-8*zbar/abar*temp*sqrt(temp)
  if (temp.le.1.0d5) drel=drel*15.0d0
  drel10=log10(drel)
  drelim=drel10+0.3d0
  dlog10=log10(den)

c..from iben apj 196 525 1975 for non-degenerate regimes
  if (dlog10.lt.drelim) then
    zdel=xne/(avo*t6*sqrt(t6))
    zdel10=log10(zdel)
    eta0=exp(-1.20322d0+twoth*log(zdel))
    eta02=eta0*eta0

c..thpl factor
  if (zdel10.lt.0.645) then
    thpl=-7.5668d0+log(zdel*(1.0d0+0.024417d0*zdel))
  else
    if (zdel10.lt.2.5) then
      thpl=-7.58110d0+log(zdel*(1.0d0+0.02804d0*zdel))
    if thpla=thpl(zdel10.ge.2.0) then
      thpl=-11.0742d0+log(zdel**2*(1.0d0+9.376d0/eta02))
      thpl=-2.0d0*((2.5d0-zdel10)*thpla+(zdel10-2.0d0)*thpl)
    end if
  end if

```

```

else
  thp1 = -11.0742d0 + log(zdel**2 * (1.0d0 + 9.376d0/eta02))
endif
endif

```

c..pefac and walf factors

```

if (zdel110 .lt. 2.0) then
  pefac = 1.0d0 + 0.021876d0*zdel
  if (zdel110 .gt. 1.5) then
    pefac1 = log(pefac)
    pefac1 = log(0.4d0*eta0 + 1.64496d0/eta0)
    cfac1 = 2.0d0 - zdel110
    cfac2 = zdel110 - 1.5d0
    pefac = exp(2.0d0 * (cfac1*pefac1 + cfac2*pefac1))
  endif
else
  pefac = 0.4d0*eta0 + 1.64496d0/eta0
endif

if (zdel110 .lt. 40.0) then
  dnefac = 1.0d0 + zdel * (3.4838d-4 * zdel - 2.8966d-2)
else
  dnefac = 1.5d0/eta0 * (1.0d0 - 0.8225d0/eta02)
endif
wpar2 = 9.24735d-3 * zdel *
1      (den*avo*(w(4)+w(5)+w(6))/xne + dnefac) / (sqrt(t6)*pefac)
walf = 0.5d0 * log(wpar2)
walf10 = 0.5d0 * log10(wpar2)

```

c..thx, thy and thc factors

```

if (walf10 .le. -3.0) then
  thx = exp(2.413d0 - 0.124d0*walf)
else if (walf10 .le. -1.0) then
  thx = exp(0.299d0 - walf*(0.745d0 + 0.0456d0*walf))
else
  thx = exp(0.426d0 - 0.558d0*walf)
endif

if (walf10 .le. -3.0) then
  thy = exp(2.158d0 - 0.111d0*walf)
else if (walf10 .le. 0.0) then
  thy = exp(0.553d0 - walf*(0.55d0 + 0.0299d0*walf))
else
  thy = exp(0.553d0 - 0.6d0*walf)
endif

if (walf10 .le. -2.5) then
  thc = exp(2.924d0 - 0.1d0*walf)
else if (walf10 .le. 0.5) then
  thc = exp(1.6740d0 - walf*(0.511d0 + 0.0338d0*walf))
else
  thc = exp(1.941d0 - 0.785d0*walf)
endif

oh = (xh*thx + xhe*thy + w(6)*third*thc) / (t6*exp(thp1))
endif

```

c..from yakovlev & urpin soviet astro 1980 24 303 and
c..potekhin et al. 1997 aa 323 415 for degenerate regimes

```

if (dlog10 .gt. drel10) then
  xmas = meff*xne**third
  ymas = sqrt(1.0d0 + xmas*xmas)
  wfac = weid*temp/ymas * xne
  cint = 1.0d0

```

```

c..ion-electron collision frequency and the thermal conductivity
    vie = iec * zbar * ymas * cint
    cie = wfac / vie

c..electron-electron collision frequency and thermal conductivity
    tpe = xec * sqrt(xne / ymas)
    yg = rt3 * tpe / temp
    xrel = 1.009d0 * (zbar / abar * den * 1.0d-6) ** third
    beta2 = xrel ** 2 / (1.0d0 + xrel ** 2)
    jy = (1.0d0 + 6.0d0 / (5.0d0 * xrel ** 2) + 2.0d0 / (5.0d0 * xrel ** 4))
1      * (yg ** 3 / (3.0d0 * (1.0d0 + 0.07414 * yg) ** 3))
2      * log((2.81d9 - 0.810 * beta2 + yg) / yg)
3      + pi ** 5 / 6.0d0 * (yg / 13.91d0 + yg) ** 4)
    vee = 0.511d0 * temp ** 2 * xmas / ymas ** 2 * sqrt(xmas / ymas) * jy
    cee = wfac / vee

c..total electron thermal conductivity and conversion to an opacity
    ov1 = cie * cee / (cee + cie)
    ov = k2c / (ov1 * den) * temp ** 3
end if

c..blend the opacities in the intermediate region
    if (dlog10 .le. drel10) then
        ocond = oh
    else if (dlog10 .gt. drel10 .and. dlog10 .lt. drelim) then
        farg = pi * (dlog10 - drel10) / 0.3d0
        ffac = 0.5d0 * (1.0d0 - cos(farg))
        ocond = exp((1.0d0 - ffac) * log(oh) + ffac * log(ov))
    else if (dlog10 .ge. drelim) then
        ocond = ov
    end if

c..total opacity
    opac = orad * ocond / (ocond + orad)
    return
end

```

REFERENCES

- Arnett, D. 1996, *Supernovae and Nucleosynthesis: An Investigation of the History of Matter, from the Big Bang to the Present* (Princeton: Princeton Univ. Press)
- Arnett, D., & Livne, E. 1994, *ApJ*, 427, 315
- Bildsten, L. 1995, *ApJ*, 438, 852
- Blinnikov, S. I., Dunina-Barkovskaya, N. V., & Nadyozhin, D. K. 1996, *ApJS*, 106, 171
- Caughlan, G. R., & Fowler, W. A. 1988, *At. Data Nucl. Data Tables*, 40, 283
- Christy, R. F. 1966, *ApJ*, 144, 108
- Frankel, M. L., & Sivashinsky, G. I. 1982, *Combust. Sci. Tech.*, 29, 207
- Fryxell, B. A., & Woosley, S. E. 1982, *ApJ*, 261, 332
- Hansen, C. J., & Kawaler, S. D. 1994, *Stellar Interiors; Physical Principles, Structure, and Evolution* (New York: Springer)
- Iben, I., Jr. 1975, *ApJ*, 196, 525
- Iben, I., Jr., Fujimoto, M. Y., & MacDonald, J. 1992, *ApJ*, 388, 521
- Itoh, N. et al. 1996, *ApJS*, 102, 411
- Khokhlov, A. M. 1988, *Ap&SS*, 149, 91
- . 1995, *ApJ*, 449, 695
- Landau, L. D., & Lifshitz, E. M. 1959, *Fluid Mechanics* (Oxford: Pergamon)
- Mazurek, T. J. 1973, *Ap&SS*, 23, 365
- Nadyozhin, D. K. 1974, *Nauchn. Inf. Astron. Soviet USSR*, 32, 3
- Nandkumar, R., & Pethick, C. J. 1984, *MNRAS*, 209, 511
- Niemeyer, J. C., & Hillebrandt, W. 1995a, *ApJ*, 452, 769
- . 1995b, *ApJ*, 452, 779
- Oran, E. S., & Boris, J. P. 1987, *Numerical Simulation of Reactive Flow* (New York: Elsevier)
- Paquette, C., et al. 1986, *ApJS*, 61, 177
- Potekhin, A. Y., Chabrier, G., & Yakovlev, D. G. 1997, *A&A*, 323, 415
- Potekhin, A. Y., & Yakovlev, D. G. 1996, *A&A*, 314, 341
- . 1999, *A&A*, in press
- Schwarzschild, M., & Härm, R. 1965, *ApJ*, 142, 855
- Timmes, F. X. 1992, *ApJ*, 390, L107
- . 1999, *ApJS*, 124, 241
- Timmes, F. X., & Arnett, D. 1999, *ApJS*, in press
- Timmes, F. X., & Niemeyer, J. C. 1999, *ApJ*, in press
- Timmes, F. X., & Swesty, F. D. 1999, *ApJS*, in press
- Timmes, F. X., & Woosley, S. E. 1992, *ApJ*, 396, 649
- Wallace, R. K., Woosley, S. E., & Weaver, T. A. 1982, *ApJ*, 258, 696
- Weaver, T. A., Zimmerman, G. B., & Woosley, S. E. 1978, *ApJ*, 225, 1021
- Yakovlev, D. G., & Urpin, V. A. 1980, *Soviet Astron.*, 24, 303